EOM-3901
Master's Thesis in
Energy and Environment in the North

Combining ENVISAT ASAR and MODIS Data to Enable Improved Snow Cover Maps

by

Håvard Uv Mjøen

June, 2008

FACULTY OF SCIENCE
Department of Physics and Technology
University of Troms

Abstract

Information about snow covered area is important for several purposes, and this information can be found by detecting reflection of optical waves using optical sensors or by using active radars such as SAR.

This thesis is explaining how information from the measurements are used to make snow maps. Optival sensors cannot detect snow when the area is covered by clouds, and this is a problem in the melting season in Norway. Microwaves can penetrate clouds, and detect wet snow. It cannot detect dry snow, but we will make snow maps based on the probability of dry snow. When we combine snow maps made from an optical instrument (MODIS) and a SAR (ENVISAT ASAR) we are able to get improved snow cover maps in times when the optical instrument cannot see the surface because of clouds.

We will study a moving average filter and the Kalman filter. These filters are used to be able to filter the information about the snow cover to get an estimate of the snow covered area for each day. When comparing the results from the moving average filter with the Kalman filter, the results indicate that the Kalman filter gives a better estimation based on the measurements.

We will also study relation between measured snow cover and the topography, and also if there are any relation between land cover and snow cover. The results indicate that the data from the optical sensors is underestimating the snow cover in northern slopes. The results also indicates that the melting of snow is correlated to the elevation.

Acknowledgment

This thesis concludes my education in energy and environment in the north at the University of Troms. I would like to express my gratitude to all the people that have supported me during this time.

First of all I would like to thank my supervisors Professor Torbjørn Eltoft, Senior Research Scientist Eirik Malnes and Senior Research Scientist Bernt Johansen for all the help and support, and for giving me an exciting task to work on. I will also thank Norut Tromsø for the techical support and all the coffee

Thanks to my fellow students and the studentorganisations Foreninga and IAESTE for the company, support and the coffee breaks.

Thanks to my family for believing in me, and for being there for me when needed.

Last but not least I would like to thank my girlfriend Stine Skrunes. Thank you for supporting me through the hardest periods and your patience with me.

Håvard Uv Mjøen
Tromsø June 2, 2008

Contents

Chapter 1

Introduction

In the northern hemisphere there is an average area of 30 to 40 million km^2 covered with snow during the winter. This snow mass is equivalent to between 2000 to 3000 km^3 of water. About 50% of the precipitation in the mountains in Norway fall as snow. All this snow affects processes that interacts between atmosphere and surface, and information about the snow covered area (SCA) is important for climatology, weather forecast, hydrology, flood warning, ecology, flora and fauna etc [20].

Since half the percipitation fall as snow in Norway, over half the annual runoff is happening in the melting season. Observation of the snow covered area will contribute to valuable information about runoff, and with this information it is possible to improve the prediction of flood. Flood is a risk both in areas with stable winter snow coverage and in areas where snow only occasionally covers the land. Hydroelectic power stations also need some information about how far the runoff has come to be able to calculate how much water they will get in their reservoirs.

Global warming is a problem that affects the snow covered area. Snow reflects radiation more effective than bare soil, and with less snow covered area because of global warming, more radiation will be absorbed by the bare ground and we get a positive feedback effect. Monitoring snow covered area could provide early evidence of a possible change in the climate [4].

Remote sensing as a technology started with the first photographs in the early nineteenth century. Under World War 1, cameras was mounted on airplanes or handheld by aviators, and provided invaluable information for military reconnaissance. Remote sensing above the atmosphere originated at the dawn of Space Age. The first satellite which returned images was the Corona mission 9009 in 1959, and the motivation in the beginning was to get information about the enemy during the cold war, but things changed. The development of sensors and digital image processing algorithms to extract important information about the land cover from remote sensed data has been devoted significant effort since the cold war. Examples of the development is multispectral images to get more specified information from the land cover, and better resolution on the ground.

Snow cover has been monitored from space using images from optical sensors since 1966 [17]. Many papers are written about optical remote sensing sensors ability for mapping the snow covered area, but they are limited by clouds and lack of daylight. In Norway, lack of daylight is a big problem for optical sensors, not only where there are polar night, but it is also a problem on the shadow-side of mountains early in the season when the sun is low. Clouds are also very common in the melting season [2, 18].

Already in the 1970's, ground based signature research clearly revealed the capabilities of X-band and C-band Syntetic Aperture Radar (SAR) for detecting wet snow [13], and since 1978 passive microwave images has been used to monitor the snow cover [17]. SAR can look through clouds, and does not need any daylight, but the C-band SAR-sensors are only sensitive to wet snow. The backscattering coeffisient is not changed much by dry snow compared to bare ground, and since SAR-images has problems with speckle and geometric distortion due to layover, foreshortening and shadowing, we can not measure dry snow directly. Several papers [3, 11, 14] has shown that it is possible to map wet snow by SAR because of the lower backscattering coeffisient of wet snow compared to bare ground. Norwegian Computing Center (NR) and Norut have together tried to combine the use of optical and SAR seonsors to get the best from both worlds. They used SAR-based maps to update the SCA maps when they were missing optical observations, and this combination gave a clearly better SCA-maps than using a single-sensor only [20].

What we will do in this thesis is to look at how SCA-maps are made from satellite measurements, and try to improve the work of NR and Norut further. We will study new ways of filtering the SCA-maps to obtain better estimates. We will especially study the Kalman filter for this purpose. We will also investigate some additional information such as meteorological measurements of the temperature, snow depth and precipitation to see if our results corresponds with the in situ measurements. Land cover maps and digital elevation models will also be used to see if there are any corrolation between snow melting and elevation and land cover.

We will also take a investigate existing problems with the algorithms that makes the SCA-maps, and topographical influence on the measurements.

1.1 Structure of this thesis

This thesis is divided into 9 chapters.

- Chapter 2 introduce the basic concept of electromagnetic waves, and how they interact with different matter. How snow interacts with electromagnetic waves is especially important.
- Chapter 3 presents the instruments used to acquire the images we will look more into.
- Chapter 4 explain the concept of the Kalman filter. A detailed description of both simple and extended Kalman filter is given, and an example of how it is used.
- Chapter 5 explains how the images from the instruments are used to obtain snow cover maps. Some problems about them are also discussed.
- Chapter 6 presents other data used in this thesis.
- Chapter 7 presents the main algorithm and the methods used to filter the snow maps.
- Chapter 8 presents and discusses the results found using the different filter and background data.
- Chapter 9 concludes this thesis and suggest some work that may be done in the future.

Chapter 2

Electromagnetic Radiation Principles

To understand how electromagnetic radiation is created, travel through space and interacts with other matter, we will describe the processes using two different models; the wave model and the particle model.

2.1 Wave Model of Electromagnetic Energy

A electromagnetic wave consists of an electric and a magnetic fluctuating field. These two fields are orthogonal to each other, and both are perpendicular to the travel direction. The relationship between the wavelength and the frequency of the wave is

$$c = \lambda\nu, \tag{2.1}$$

where c is the speed of light, λ is the wavelength and ν is the frequency.

Electromagnetic energy is emitted from all objects with a temperature above absolute zero (-273^oC or 0 K). This includes water, soil, rock, vegetation and the surface of the sun. The sun is the source of most of the electromagnetic energy recorded by remote sensing systems, including MODIS. A black body is a theoretical object that absorbs all electromagnetic radiation that falls onto it, and re-emitts the energy at maximum possible rate per unit area at each wavelength λ for a given temperature. The Sun can be thought of as a black body with a temperature of $5770 - 6000$ K. The total emitted radiation from a black body can be expressed as

$$M_\lambda = \sigma T^4, \tag{2.2}$$

where σ is the Stefan-Boltzmann constant, $5.6697 \times 10^{-8} W m^{-2} K^{-4}$, and T is the temperature measured in kelvin (K). To calculate the dominant wavelength (λ_{max})

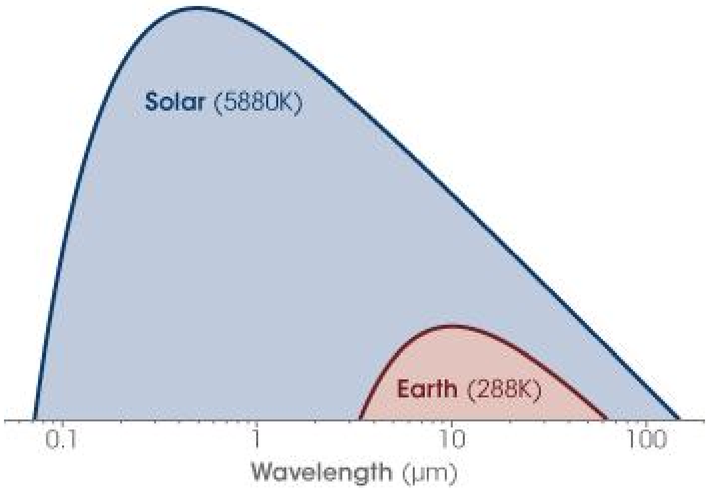

Figure 2.1: Black body radiation for different temperatures. The Sun has an approximated temperature of 5880 K, while the earth has a temperature of 288 K. Illustration borrowed from [24].

we use Wien's displacement law:

$$\lambda_{max} = \frac{k}{T}, \tag{2.3}$$

where k is a constant equal to 2898μm K. From this equation we find that the dominant wavelength for the Sun is 0.493μm, which is blue/green light, while the Earth has a dominant wavelength of 10.1μm, which is in the thermal infrared region.

2.2 Particle Model of Electromagnetic Energy

Albert Einstein found that when light interacts with electrons, it could not be explained as a wave. He concluded that light had mass that he called photons, which has an energy and momentum. The electrons in an atom is located in different energy levels, and if a photon is absorbed by the atom, the electron will be excited to a higher energy level. After 10^{-8} seconds the electron falls back to a lower empty energy level, and it emitts a new photon. The difference between the energies in the two levels is the same as the energy of the photon absorbed or emitted. If the electron falling to a lower energy level do this in several steps, it will send out a photon every time, and the sum of the energy will be the same as the difference between the excited and the normal energy levels.

The relationship between the wavelength (λ) and the energy (Q) in the photon is

$$Q = h\nu, \tag{2.4}$$

where h is the Planck constant, 6.626×10^{-34}Js. When we substitute ν with equation 2.1 we get

$$Q = \frac{hc}{\lambda} \tag{2.5}$$

or

$$\lambda = \frac{hc}{Q} \tag{2.6}$$

From equation 2.6 we see that the wavelength (λ) is inversely proportional with the enerqy (Q). This implies that it is harder to detect radiation with longer wavelength than radiation with shorter.

2.3 Reflectance of Electromagnetic Energy

When energy from the sun strikes an object, there are five possible interactions. The energy can be [25]:

- Transmitted. The energy passes through the object with a change of velocity determined by the index of refraction for the two media in question.
- Absorbed. The object takes the energy through an electron or molecular reaction.
- Reflected. The object works like a mirror and returns the energy unchanged with the angle of reflection equal to the angle of incidence. Reflectance is the ratio between reflected energy and the incident energy on the body. The reflected wavelength determines the color of the object.
- Scattered. The direction of energy propagation is randomly changed. Rayleigh- and Mie-scatter are the most important types of scatter in the atmosphere.
- Emitted. The energy which is absorbed is later re-emitted, usually at longer wavelegths. The object also heats up.

There are several types of reflecting surfaces. When the surface where the radiation is reflected is smooth we get specular reflection. We can often see this phenomena when we look at calm water and see the reflection in the water. If the surface is more rough, the reflected radiation goes in several directions, and we get a diffuse reflectation or scattering. A perfect diffuse reflector is called a

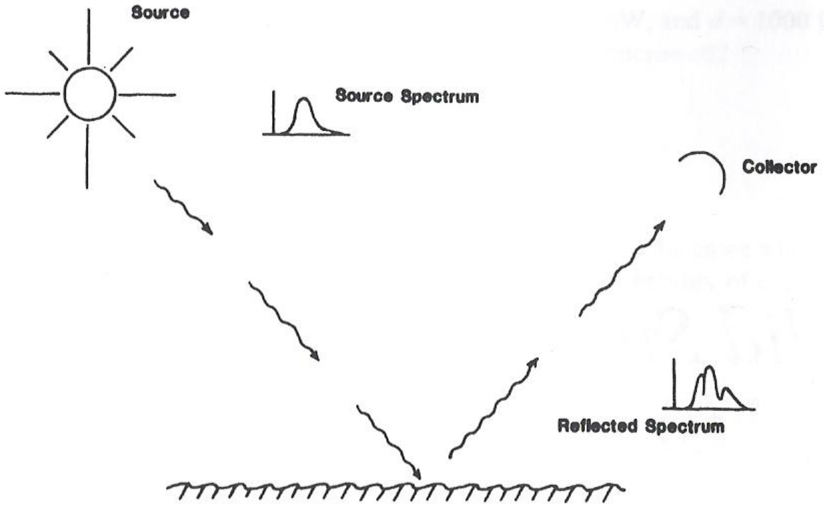

Figure 2.2: The surface spectral imprint is reflected in the specter of the reflected waves. Illustration borrowed from [5].

Lambertian surface, and the radiant flux leaving the surface is constant for any angle of reflectance [8].

The characteristics of the reflected radiant flux is very importnant in remote sensing. If we know how much and which wavelength is absorbed and reflected, we can get important information about the terrain we are measuring. The total amount of radiant flux $\Phi(\lambda)$ in a specific wavelength (λ) has to be accounted for by taking the sum of the total amount of reflected radiant flux, $\Phi_r(\lambda)$, absorbed radiant flux, $\Phi_a(\lambda)$, and transmitted radiant flux, $\Phi_t(\lambda)$;

$$\Phi(\lambda) = \Phi_r(\lambda) + \Phi_a(\lambda) + \Phi_t(\lambda) \tag{2.7}$$

We can see an example of this in figure 2.2. The reflected spectrum is different from the source spectrum because some of the frequencies are absorbed or transmitted more than others. The hemispherical reflectance (ρ_λ) is defined as the ratio between reflected radiant flux from the surface and the radiant flux incident to it;

$$\rho(\lambda) = \frac{\Phi_r(\lambda)}{\Phi(\lambda)} \tag{2.8}$$

This can also be expressed as a percent:

$$\rho_{\%}(\lambda) = \frac{\Phi_r(\lambda)}{\Phi(\lambda)} \times 100 \tag{2.9}$$

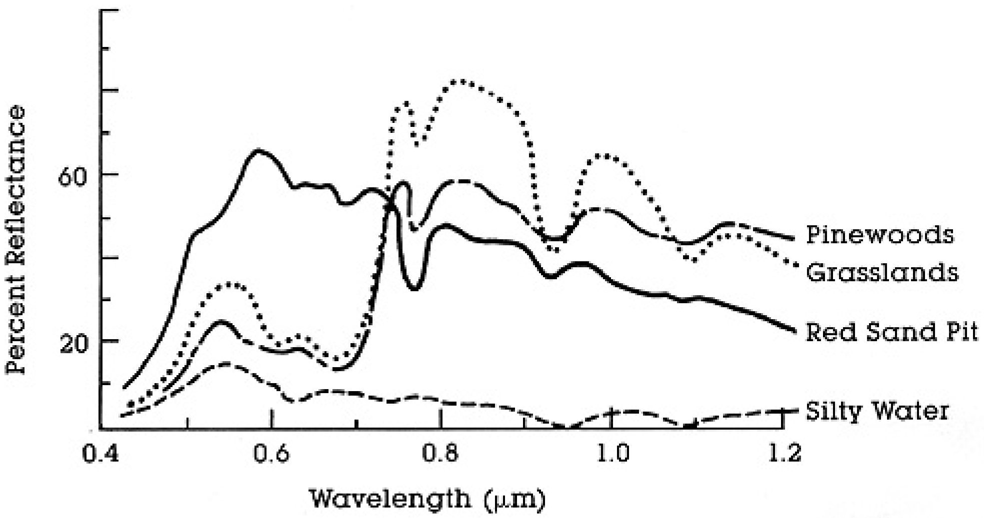

Figure 2.3: Spectral reflectance curves of four different targets. Illustration borrowed from [25].

This is often used in remote sensing research to describe the spectral reflectance characteristics of various phenomena. If we look at figure 2.3, we see that the red sand pit reflects about 60% of the energy at about 0.6μm, while the other three only reflects about $10 - 20\%$. Silty water is just as easy to distinguish with a low reflectance for all wavelengths. Pinewoods and grasslands has more similar curves, but if we measure the reflectance at 0.85μm and 1.0μm we should be able to see the differance.

2.4 Radiant Flux Density

Equation 2.8 does not provide any information about the direction the reflected energy is exiting. To be able to do that we need to specify the amount of radiant flux leaving a surface per unit area, also called exitance:

$$M(\lambda) = \frac{\Phi_r(\lambda)}{A}, \tag{2.10}$$

where A is the area of the reflecting surface. Even if we include information about the size of the surface we still don't know the radiant flux in any direction from the surface.

Radiance (L) is the radiant intensity per unit of projected source area in a specified direction. We are only interested in the radiance in one direction, so we

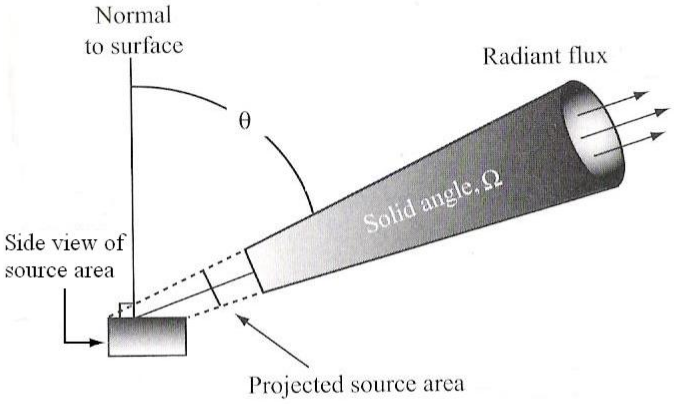

Figure 2.4: The concept of radiance leaving a specific projected source area on the ground, in a specific direction and within a specific solid angle. Illustration borrowed from [8].

evaluate the figure 2.4. We are only after the radiance from the projected source area ($Acos\theta$) in the solid angle Ω:

$$L(\lambda) = \frac{\frac{\Phi_r(\lambda)}{\Omega}}{Acos\theta} \tag{2.11}$$

The radiance we measure from a satellite will be different than this theoretical L because of atmospherical interactions, such as scattering.

2.5 Electomagnetic reflectance of snow

Compared to most vegetation, soil and water, snow have a much higher reflectance in the visible wavelengths. The reason for the high reflectance lies in the dielectric properties of ice and in the fact that snow is composited by ice in a very highly divided form of the order 10^9 particles per cubic meter. The high reflectance in all visible band compared to other land covers makes it relatively straightforward to classify snow based on optical instruments.

The problem in classification snow is clouds. The reflectance spectre of snow and clouds can be seen in figure 2.5, and we can see they have a similar reflectance in the visible wavelength. To be able to distinguish the two, we can either use several images taken within a relatively short period, and look for movements since clouds moves and snow does not, or we can check the reflectance in a wavelength where snow and clouds are very different from eachother. At about 1,6 μm clouds has a reflectance at about 50% while snow has a reflectance near 0%, and this difference will make the classification easier.

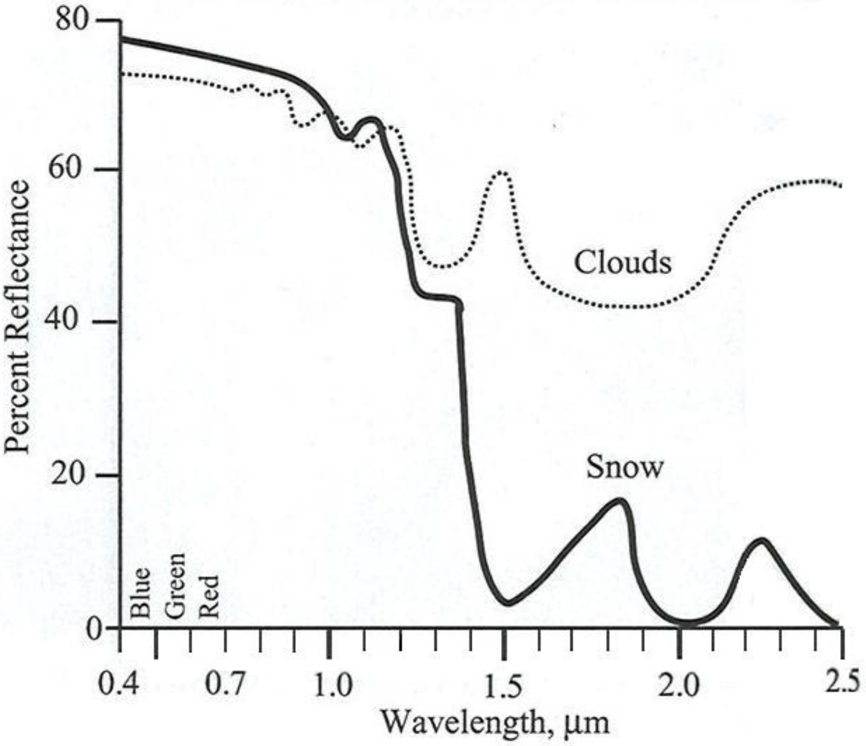

Figure 2.5: Reflactance of clouds and snow in the the wavelength interval 0,4 to 2,5 μm. Illustration borrowed from [8].

The ASAR instrument use the C-band channel to retrieve information about the snow cover. The reflection of radiation from a planar snow surface is determined by the difference in the dielectric constant of the snow and the external medium (air) and the angle at which the radiation strikes the snow. The greater difference in dielectric constand, the greater reflection coeffisient.

The scattering from any surface is depending on the dielectric constant of the surface, its roughness properties and the geometry of the scattering. The real part of the dielectric constant of ice is practically constant for all frequencies in the microwave region. The degree of absorption is determined of the imaginary part of the dielectric constant, and for dry snow it is very small. Since there is a low degree of absorption in dry snow, propagation of microwaves are generally dominated by scattering. Visible wavelength are shorter than the grain size, and that makes them scatter in a high degree, and the snow seems white for our eyes. But microwaves are much longer than the grain size, and this make the attenuation lenght fairly long. As a consequence of this, dry snow can be almost transparent unless they are deep, giving a backscattering coefficient that is essentially that of

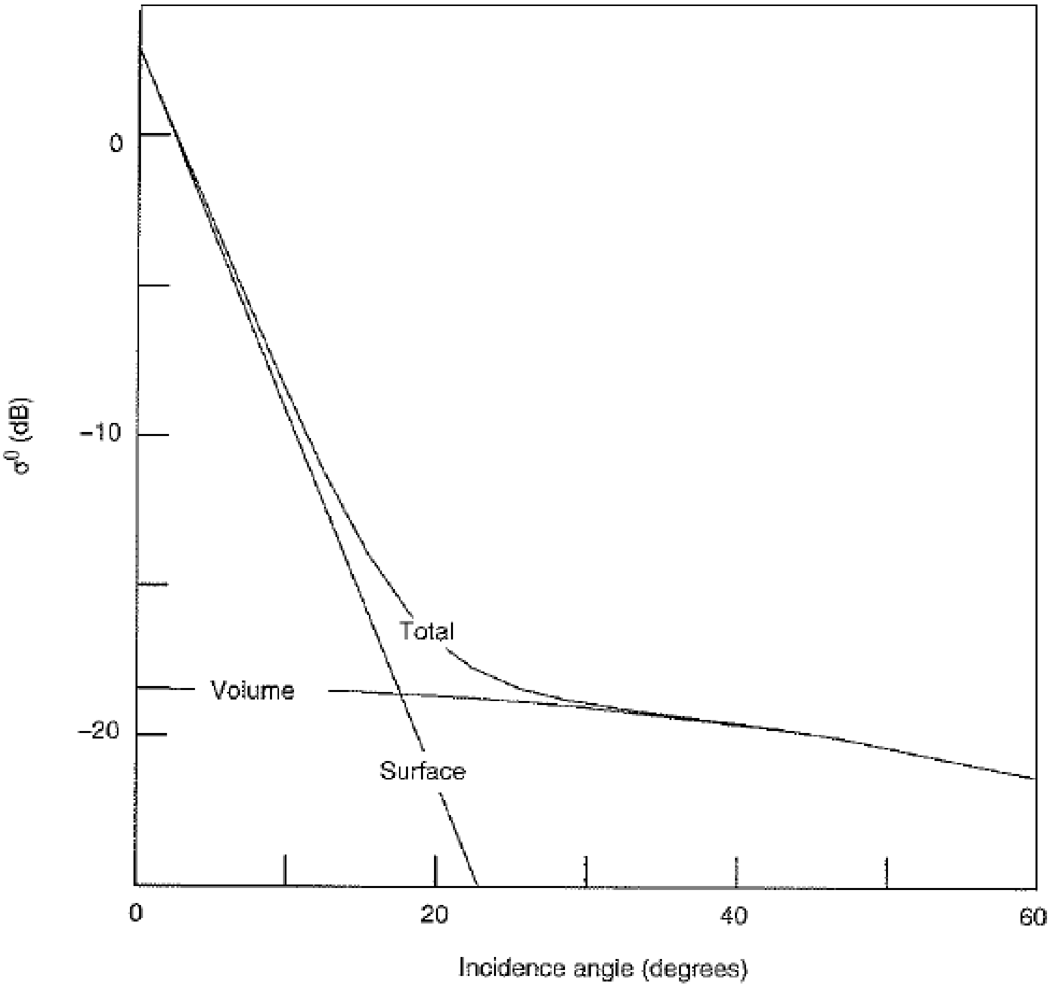

Figure 2.6: Typical variation of copolarized backscattering coefficient with incidence angle for wet snow (schematic). Illustration borrowed from [17].

the underlaying surface.

The backscatter of wet snow containes contributions from both surface and volume scattering. Figure 2.6 show the typical relation between backscattering coefficient and the incidence angle. The backscatter is dominated by scatter from the surface for incidence angles below 17°, and volume scatter for angles greater than this. Volume scatter has little variation with incidence angle, and since C-band SAR are typically measuring the backscatter at an incidence angle of 23° we can see from figure 2.6 that the backscatter coefficient is very low [17]. A low backscatter coefficient is a clear indication of wet snow, and can be used to extract information about the snow cover as we will look more into in section 5.2.

Chapter 3

Instruments

3.1 Advanced Synthetic Aperture Radar (ASAR)

The ENVISAT Advanced Synthetic Aperture Radar (ASAR) is one of the 10 instruments on board of ENVISAT (Environmental Satellite). It was launched on March 1, 2002. It has a Sun synchronous polar orbit at height 790 km, and orbits the earth in 101 minutes, with a repeat cycle of 35 days. The ASAR on board of ENVISAT extends the mission of the Active Microwave Instrument (AMI) Syntetic Aperture Radar (SAR) instruments flown on the ERS-1 and ERS-2 satellites.

ASAR use an active phased-array antenna with possible incidence angles between 15 and 45°, and it operates in the C-band. We use output from the Wide Swath mode, which give us a swath width of 400km and a spatial resolution of 150 × 150 meters.

The pulse sent by the ASAR is a chirp to allow the pulse to be much longer. A long pulse allow more energy to be emitted, and hence recieved. I longer pulse usually hinders range resolution, but a chirp has a frequency shift during the pulse, and when this pulse is returned it must be correlated with the sent pulse.

The chirped pulse from the ASAR antenna will be broad because a narrow beam needs a large antenna. The pulse will hit the terrain beneathe the antenna, and the reflected beam will return to the antenna. If the terrain is flat, the pulse will not hit the terrain at the same time since it will need to travel further to hit the terrain at a bigger incidence angle, and therefore the pulses from different distances from the flight track may be distinguished. To distinguishe points along the ground track, we can use the doppler shift. A point ahead of the ASAR returns a Doppler upshifted signal, while a point behind the ASAR returns a Doppler downshifted signal.

3.2 Moderate Resolution Imaging Spectroradiometer (MODIS)

The Moderate Resolution Imaging Spectroradiometer (MODIS) is a scientific instrument which is a payload on board of NASA's EOS Terra (10:30 a.m. descending node) and Aqua (1:30 p.m. ascending node). Terra was launched on Desember 18, 1999, and the first image from MODIS was recieved the February 24, 2000. Aqua was launched on May 4, 2002. MODIS was designed to provide measurements in large-scale global dynamics including changes in Earth's cloud cover, radiation budget and processes occurring in the oceans, on land, and in the lower atmosphere.

MODIS is in a 705 km sun-synchronous orbit, and has a double-sided scan mirror to scan a ±55° scanning pattern, with a 20,3 rpm cross track. which gives a swath width of 2330 km cross track and a 10 km swath width along track at nadir. This means the whole surface of the earth is covered every one or two days in 36 discrete spectral bands [26]. As we see in table 3.1, the bands spatial resolution ranges from 250 × 250 m to 1 × 1 km. Although other imaging systems such as the Landsats Enhanced Thematic Mapper Plus has a higher resolution (30 × 30 m), this system can only image a given area every 16 days. This is too infrequently to capture many of the rapid biological and meteorological changes that MODIS observes.

Table 3.1: Overview over the characteristics of the MODIS onbord of the Terra satellite.

Band	Wavelength (nm)	Resolution (m)
1	620 - 670	250 × 250 m
2	841 - 876	250 × 250 m
3	459 - 479	500 × 500 m
4	545 - 565	500 × 500 m
5	1 230 - 1 250	500 × 500 m
6	1 628 - 1 652	500 × 500 m
7	2 105 - 2 155	500 × 500 m
8	405 - 420	1000 × 1000 m
9	438 - 448	1000 × 1000 m
10	483 - 493	1000 × 1000 m
11	526 - 536	1000 × 1000 m
12	546 - 556	1000 × 1000 m
13	662 - 672	1000 × 1000 m
14	673 - 683	1000 × 1000 m
15	743 - 753	1000 × 1000 m
16	862 - 877	1000 × 1000 m
17	890 - 920	1000 × 1000 m
18	931 - 941	1000 × 1000 m
19	915 - 965	1000 × 1000 m
20	3 660 - 3 840	1000 × 1000 m
21	3 929 - 3 989	1000 × 1000 m
22	3 929 - 3 989	1000 × 1000 m
23	4 020 - 4 080	1000 × 1000 m
24	4 433 - 4 498	1000 × 1000 m
25	4 482 - 4 549	1000 × 1000 m
26	1 360 - 1 390	1000 × 1000 m
27	6 535 - 6 895	1000 × 1000 m
28	7 175 - 7 475	1000 × 1000 m
29	8 400 - 8 700	1000 × 1000 m
30	9 580 - 9 880	1000 × 1000 m
31	10 780 - 11 280	1000 × 1000 m
32	11 770 - 12 270	1000 × 1000 m
33	13 185 - 13 485	1000 × 1000 m
34	13 485 - 13 785	1000 × 1000 m
35	13 785 - 14 085	1000 × 1000 m
36	14 085 - 14 385	1000 × 1000 m

Chapter 4

The Kalman filter

The Kalman filter is a set of mathematical equations that estimate the state of a dynamic system from a series of incomplete and noisy measurements. It was developed by R. E. Kalman in 1960, but has been further developed since then. The filter supports estimations of past, present and future states, and it can do this even without knowing the precise nature of the modeled system. This makes the Kalman filter very powerful. The literature about the Kalman filters are covered by bib:kalman, bib:ekf and bib:kalman2.

4.1 Simple Kalman filter

Kalman's original formulation is now called *simple* Kalman filter. The filter tries to estimate the state $x \in \Re^n$ of a discrete time controlled process. The equation describing the state x_k is

$$x_k = Ax_{k-1} + Bu_{k-1} + w_{k-1}, \tag{4.1}$$

where A is a $n \times n$ matrix which relates the previous state x_{k-1} to the new state, B is a $n \times l$ matrix and is the control-input model which is applied to the optional control vector u_{k-1} and w_{k-1} is the process noise. The equation describing the measurement $z \in \Re^m$ is

$$z_k = Hx_k + v_k, \tag{4.2}$$

where H is a $m \times n$ matrix which maps the true state vector x_k into the observed vector z_k. v_k is the measurement noise. The matrices A and H might change with each step, but in simple Kalman filter we assume they are constant.

The process noise and the measurement noise are assumed to be independent, white Gaussian noise with probability distributions

$$\begin{aligned} p(w) &\sim N(0, Q), \\ p(v) &\sim N(0, R). \end{aligned} \tag{4.3}$$

In real life, the process noise covariance Q and the measurements noise covariance R matrices can change for each time step or measurement, but in the simple Kalman filter we assume they are constant. The measurement noise covariance R is usually measured before we run the filter, while the process noise covariance Q usually is very difficult to measure, since we usually cannot directly observe the process. It is often possible to "tune" both parameters by choosing them rationally and run the filter a few times to test.

$\hat{x}_k^- \in \Re^n$ is the a priori state estimate at the step k, when we have knowledge of the process prior to step k. $\hat{x}_k \in \Re^n$ is defined to be the a posteriori state estimate at step k when we have the measurement z_k. The a priori and a posteriori estimate errors are defined as

$$\begin{aligned} e_k^- &\equiv x_k - \hat{x}_k^-, \text{and} \\ e_k &\equiv x_k - \hat{x}_k. \end{aligned} \tag{4.4}$$

The estimated a priori error covariance and a posteriori error covariance is then

$$\begin{aligned} P_k^- &= E[e_k^- e_k^{-T}], \text{and} \\ P_k &= E[e_k e_k^T]. \end{aligned} \tag{4.5}$$

The predicted measurement $\hat{z}_k$ based on the a priori estimate is

$$\begin{aligned} \hat{z}_k &= E[H\hat{x}_k^- + v_k] \\ &= E[H\hat{x}_k^-] + E[v_k] \\ &= H\hat{x}_k^-, \end{aligned} \tag{4.6}$$

where $E[\hat{z}_k]$ is the expected value of $\hat{z}_k$

To derive the equations for the Kalman filter, we start with an equation that computes the a posteriori state estimate $\hat{x}_k$ as a linear combination of an a priori estimate $\hat{x}_k^-$ and a weighted difference between an actual measurement z_k and the measurement prediction $H\hat{x}_k$;

$$\hat{x}_k = \hat{x}_k^- + K(z_k - H\hat{x}_k^-). \tag{4.7}$$

The difference between the measurement and the predicted measurement $(z_k - H\hat{x}_k^-)$ is called the innovation or residual. We can justify equation 4.7 by looking at the a priori estimate $\hat{x}_k^-$, which is based on all prior measurements z_k. For now let it suffice to point out that the Kalman filter maintains the first two moments od the state distribution,

$$E[x_k] = \hat{x}_k \tag{4.8}$$

$$E[(x_k - \hat{x}_k)(x_k - \hat{x}_k)^T] = P_k. \tag{4.9}$$

If the conditions in equations 4.3 are met, the a posteriori state estimate in equation 4.7 reflects the mean of the state distribution. The state estimate error covariance in equation 4.5 reflects the variance of the state distribution. In other words;

$$\begin{aligned} p(x_k|z_k) &\sim N(E[x_k], E[(x_k - \hat{x}_k)(x_k - \hat{x}_k)^T]) \\ &= N(\hat{x}_k, P_k) \end{aligned} \tag{4.10}$$

The K in equation 4.7 is a $n \times m$ matrix. It is called the Kalman gain and is a blending factor that minimizes the a posteriori error covariance in equation 4.5. One form of the resulting K that minimizes the a posterioeri error covariance is given by [22]

$$K_k = P_k^- H^T (H P_k^- H^T + R)^{-1}. \tag{4.11}$$

If we look at equation 4.11, the residual is more importent the smaller the measurement error covariance R is;

$$\lim_{R \to 0} K_k = H^{-1}. \tag{4.12}$$

That means the measurement z_k is trusted more the smaller the measurement error covariance R is. If $R \gg P_k^-$ or the a priori error covariance estimate P_k^- is approaching zero, the gain K weights the residual less;

$$\lim_{P_k^- \to 0} K_k = 0. \tag{4.13}$$

That means the measurement z_k is trusted less the smaller the a priori esitmate error covariance P_k^- is.

4.1.1 Time update (”predict”)

The Kalman filter cycles between the time update and the measurement update. The first stop is the time update, which use the current state to estimate the a priori state and covariance. Equation 4.1 is used to predict the a priori state $\hat{x}_k^-$. Since $E[w_{k-1}] = 0$, we get

$$\hat{x}_k^- = A\hat{x}_{k-1}^- + Bu_{k-1}. \tag{4.14}$$

The predicted covariance estimate P_k^- is updated with the process noise covariance Q;

$$P_k^- = AP_{k-1}A^T + Q, \tag{4.15}$$

where A is taken from equation 4.1.

4.1.2 Measurement update (”correct”)

The measurement update updates the state when a new measurement is done based on the measurement. There are three equations in this update;

$$K_k = P_k^- H^T (H P_k^- H^T + R)^{-1}, \tag{4.16}$$

$$\hat{x}_k = \hat{x}_k^- + K(z_k - H\hat{x}_k^-), \text{and} \tag{4.17}$$

$$P_k = (I - K_k H) P_k^- . \tag{4.18}$$

The equation 4.16 estimates the Kalman gain, 4.17 estimates the a posteriori state and 4.18 estimates the a posteriori error covariance. Equation 4.16 is the same as equation 4.11 and equation 4.17 is the same as equation 4.7.

Since the Kalman filter is a cycle, the process is repeated after the measurement update. It will go on until there are no more measurements.

4.1.3 Problems with the simple Kalman filter

The problem with the simple Kalman filter is that there are several fixed parameters. The covariance matrix of the measurement noise, R can change with time, or with the instrument. If we measure the same thing with two different instruments like MODIS and ASAR, the two measurements can have different R. Also the process noise covariance Q can vary with time. An example of this could be that the process noise Q when measuring the position of a car travelling on a straight road ($x(t) \in \Re$ and $Q \in \Re$), is smaller when the velocity of the car is smaller. The relation between last and new state, A, might neither be constant. An example of this is the position of a car which is accelerating.

4.2 Extended Kalman filter

The extended Kalman filter solves some of the problems with the simple Kalman filter. It can handle a process with a non-linear stochastic difference equation by linearizing about the current mean and covariance. To be able to do this we have to modify our equations.

The state $x \in \Re^n$ is now given by the non-linear stochastic difference equation

$$x_k = f(x_{k-1}, u_{k-1}, w_{k-1}). \tag{4.19}$$

The function f is non-linear, and relates the previous state x_{k-1} to the new state x_k. u_k is an optional control-input as in the simple Kalman filter.

The measurement $z \in \Re^m$ is now described by

$$z_k = h(x_k, v_k). \tag{4.20}$$

The function h is a non-linear function which relates the actual state x_k with the measurement z_k. w_k and v_k still represent the random process and measurement noise with zero means, but the noise covariances are dependent on k;

$$\begin{aligned} p(w_k) &\sim N(0, Q_k), \\ p(v_k) &\sim N(0, R_k). \end{aligned} \tag{4.21}$$

Since $E[w_k] = 0$ and $E[v_k] = 0$, we can approximate the states and measurements as

$$\tilde{x}_k = f(\hat{x}_{k-1}, u_{k-1}, 0), \text{and} \tag{4.22}$$

$$\tilde{z}_k = h(\tilde{x}_k, 0). \tag{4.23}$$

$\hat{x}_{k-1}$ is the a posteriori state estimate from the previous step.

We have to linearize the equations 4.19 and 4.20 to be able to estimate the non-linear process. We get

$$x_k \approx \tilde{x}_k + A(x_{k-1} - \hat{x}_{k-1}) + W w_{k-1}, \text{and} \tag{4.24}$$

$$z_k \approx \tilde{z}_k + H(x_k - \tilde{x}_k) + V v_k, \tag{4.25}$$

where

- A is the Jacobian matrix of partial derivatives of f with respect to x;

$$A_{[i,j]} = \frac{\partial f_{[i]}}{\partial x_{[j]}}(\hat{x}_{k-1}, u_{k-1}, 0),$$

- W is the Jacobian matrix of partial derivatives of f with respect to w;

$$W_{[i,j]} = \frac{\partial f_{[i]}}{\partial w_{[j]}}(\hat{x}_{k-1}, u_{k-1}, 0),$$

- H is the Jacobian matrix of partial derivatives of h with respect to x;

$$H_{[i,j]} = \frac{\partial h_{[i]}}{\partial x_{[j]}}(\tilde{x}_k, 0), \text{and}$$

- V is the Jacobian matrix of partial derivatives of h with respect to v;

$$V_{[i,j]} = \frac{\partial h_{[i]}}{\partial v_{[j]}}(\tilde{x}_k, 0).$$

All these quantities are varying with each step k, but for simplisity, the k-dependency has been supressed.

From equation 4.19 and 4.22 we can calculate the prediction error as

$$\tilde{e}_{x_k} = x_k - \tilde{x}_k, \tag{4.26}$$

while the measurement error, or residual will be

$$\tilde{e}_{z_k} = z_k - \tilde{z}_k. \tag{4.27}$$

It is not possible to calculate the prediction error in equation 4.26 since we have no information about x_k. We know the measurement z_k, and with this we can rewrite equation 4.26 and 4.27 into

$$\tilde{e}_{x_k} \approx A(x_{k-1} - \hat{x}_{k-1}) + \epsilon_k, \tag{4.28}$$

$$\tilde{e}_{x_k} \approx H\tilde{e}_{x_k} + \eta_k, \tag{4.29}$$

where ϵ_k and η_k are independent random variables with distributions

$$p(\epsilon_k) \sim N(0, WQ_kW^T), \text{and} \tag{4.30}$$

$$p(\eta_k) \sim N(0, VR_kV^T). \tag{4.31}$$

Since we cannot calculate the actual prediction error, we can calculate the a posteriori prediction error $\hat{e}_{x_k}$ using the a posteriori state $\hat{x}_k$ instead;

$$\hat{e}_{x_k} = \hat{x}_k - \tilde{x}_k. \tag{4.32}$$

This can also be written by using the Kalman gain K_k;

$$\hat{e}_{x_k} = K_k\tilde{x}_{z_k}. \tag{4.33}$$

If we substitute equation 4.33 into 4.32 we get

$$\begin{aligned} \hat{x}_k &= \tilde{x}_k + K_k\tilde{x}_{z_k} \\ &= \tilde{x}_k + K_k(z_k - \tilde{z}_k), \end{aligned} \tag{4.34}$$

which can be used for the measurement update in the extended Kalman filter. $\tilde{x}_k$ and $\tilde{z}_k$ is taken from equation 4.22 and 4.23 respectively.

4.2.1 Time update (”predict”)

We have now got all equations needed to run the extended Kalman filter. As in the simple Kalman filter we have a time update and a measurement update which runs in a cycle until there are no more measurements. To get the a priori state estimate we use equation 4.22 but substitute $\hat{x}_k^-$ for $\tilde{x}_k$ to keep the same notation as in the simple Kalman filter. The equations for the time update is

$$\hat{x}_k^- = f(\hat{x}_{k-1}, u_{k-1}, 0), \text{and} \tag{4.35}$$

$$P_k^- = A_k P_{k-1} A_k^T + W_k Q_{k-1} W_k^T, \tag{4.36}$$

where P_k^- is the predicted covariance estimate.

4.2.2 Measurement update (”Correct”)

The measurement z_k is used in the measurement update to correct the state and covariance estimates. These three equations is very siminar with the ones for the measurement update for the simple Kalman filter;

$$K_k = \frac{P_k^- H_k^T}{H_k P_k^- H_k^T + V_k R_k V_k^T} \tag{4.37}$$

$$\hat{x}_k = \hat{x}_k^- + K_k(z_k - h(\hat{x}_k^-, 0)) \tag{4.38}$$

$$P_k = (I - K_k H_k) P_k^- \tag{4.39}$$

4.3 Example of the Kalman filter

An example where the Kalman filter can be used is when measuring the velocity of a car moving straight forward at constant speed. We measure the velocity with a corrupt instrument, which add a white Gaussian noise with mean 0 and variance 1 to the actual value. This example can be solved using a simple Kalman filter with the state $x_k \in \Re$. Our process can be explained by the equation

$$\begin{aligned} x_k &= A x_{k-1} + B u_{k-1} + w_{k-1} \\ &= x_{k-1} + w_{k-1} \end{aligned} \tag{4.40}$$

Since the car is moving with a constant velocity, the relation between new and previous state $A = 1$. We use no control input so $u = 0$. w is the process noise ($w \sim N(0, Q)$). The measurements $z_k \in \Re$ can be explained by the equation

$$\begin{aligned} z_k &= H x_k + v_k \\ &= x_k + v_k. \end{aligned} \tag{4.41}$$

Our noisy instrument measure the state directly, so $H = 1$. v_k is the measurement noise which is given by $v_k = N(0, 1)$.

4.3.1 The filter equations and paramters

The time update for this example can be written as

$$\hat{x}_k = \hat{x}_{k-1}^-, \text{and} \tag{4.42}$$

$$P_k^- = P_{k-1} + Q. \tag{4.43}$$

The equaion for the measurement update is

$$K_k = P_k^-(P_k^- + R)^{-1} \tag{4.44}$$

$$\hat{x}_k = \hat{x}_k^- + K_k(z_k - \hat{x}_k^-) \tag{4.45}$$

$$P_k = (1 - K_k)P_k^- \tag{4.46}$$

We presume the process variance is small $Q = 0,005$. We could presume it is zero, but a small process noise will give us more flexibility in tuning the filter.

The initial values needs to be set, and since we from equation 4.41 have that $E[x_k] = z_k$, we set the initial state $\hat{x}_0 = z_0$. We also need to choose the initial value for P_0. If we were absolutley certain that our initial state estimate $\hat{x}_0 = z_k$ was correct we could set $P_0 = 0$, but if we look at equation 4.44 and 4.45 we see that the filter always will believe that $\hat{x}_k \approx z_0$. The selection of P_0 is not that important, because P_0 will converge to it's actual value over time. We start our filter with $P_0 = 1$.

4.3.2 Simulation of the filter

To get some data to simulate we choose the actual velocity of the car to be $x = 1$m/s. 60 measurements z_k are simulated with the measurement noise $v_k \sim N(0, 1)$ added. The measurements noise variance is set to $R = 1$ since that is what the actual measurement error variance. To show why this is a good choice we will also run the same measurements with a filter with $R = 5$ and $R = 0, 1$.

Figure 4.1 shows the result from the first simulation with $R = 1$ and and $P_0 = 1$. As said, the selection of P_0 is not important, and figure 4.2 shows that P_k converge towards approximately 0,07. Figure 4.3 shows the same simulation when we choose $P_0 = 0, 07$. It is easy to see it is slower in the beginning, but after about 50 seconds it is at the same level as figure 4.1.

Equation 4.12 tells us that the filter trusts the measurement z_k more when the measurement noise variance R is small. If the measurement noise variance R is larger, the measurements will be trusted less. Figure 4.4 shows the filter simulations with a higher measurement noise variance $R = 5$ with a calibrated P_0. If we compare this figure with figure 4.3 we see that the filter with higher measurement noise variance is slower, and does not react as much on each measurement. Figure

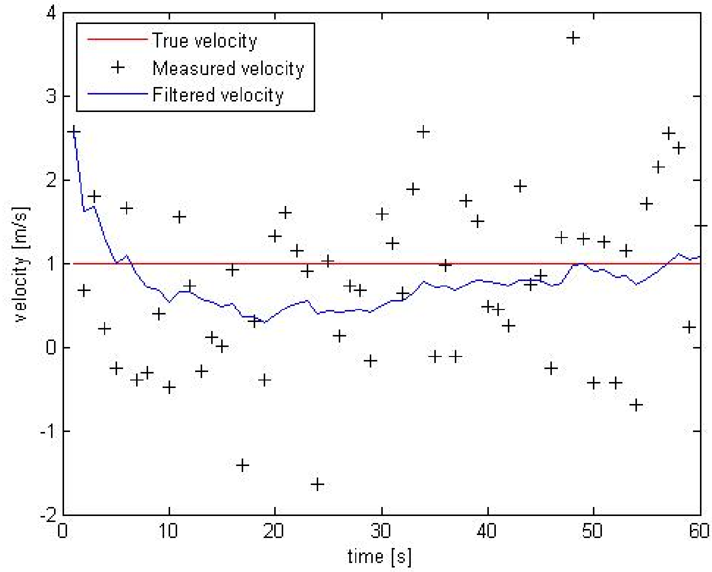

Figure 4.1: The simulation with $R = 1$ and and $P_0 = 1$. The true value of the velocity is $x = 1$. We see the filter estimate alternate around the actual state.

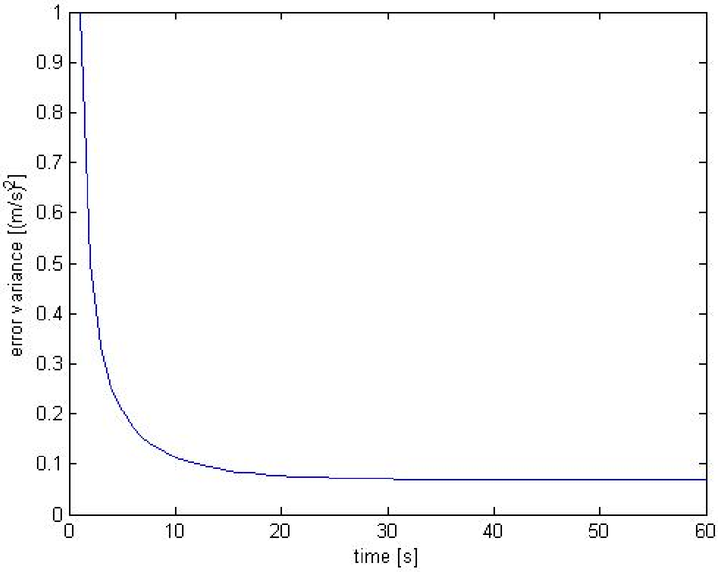

Figure 4.2: The simulated error variance with $R = 1$ and $P_0 = 1$. We see the error variance has settled at about 0,07 after 60 iterations.

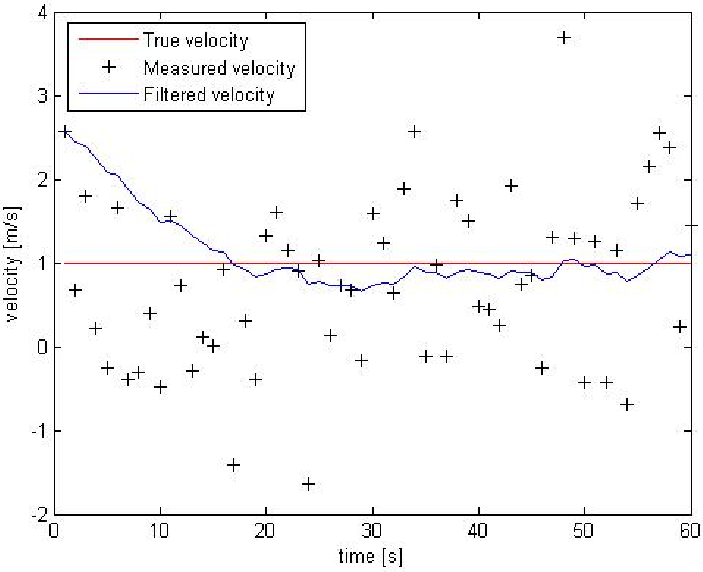

Figure 4.3: The simulation with $R = 1$ and $P_0 = 0.07$.

4.5 shows the filter with a measurement noise variance $R = 0,1$ and a calibrated P_0. This filter is very fast and reacts very fast on each measurement. It is evident that a lot of the noise is not removed, and that the estimator not will relaxate towards the right value.

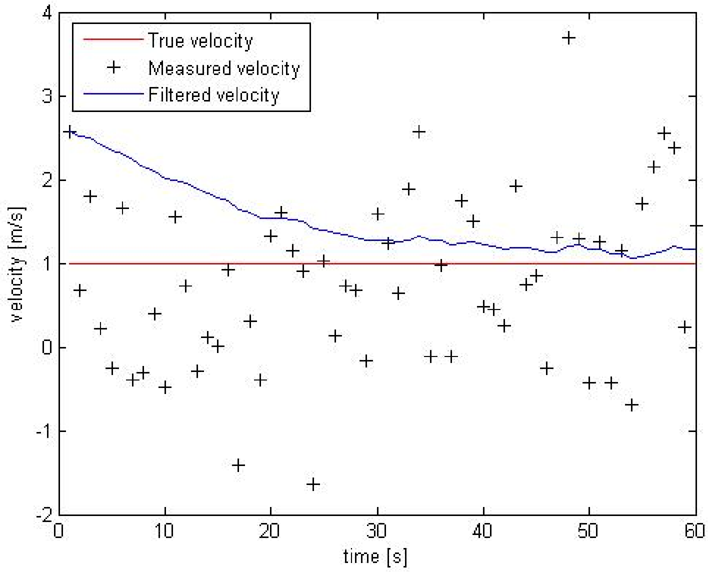

Figure 4.4: The simulation with $R = 5$. P_0 is calibrated for the specific R. The filter resonds slower to the measurements.

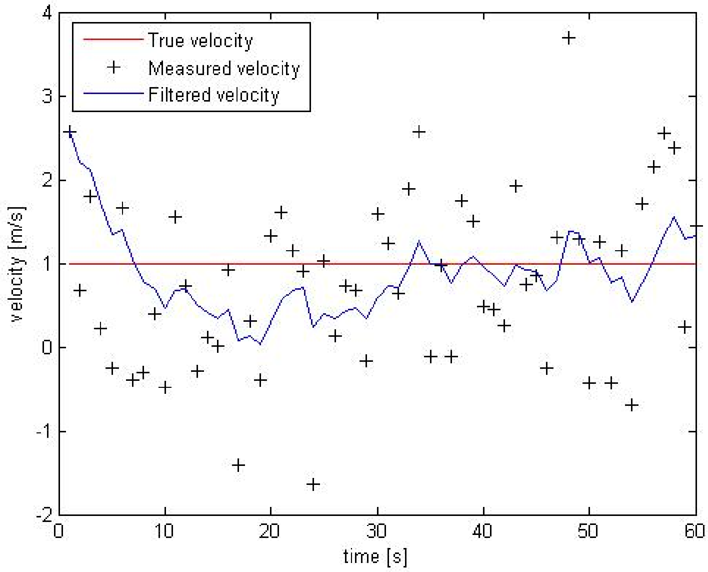

Figure 4.5: The simulation with $R = 0,1$. P_0 is calibrated for the specific R. The filter responds quickly to the measurements.

Chapter 5

Snow cover retrieval algorithms applied

5.1 Optical algorithm

The basis of the optical snow covered area algorithm is the reflectance-to-snow-cover model [2, 18]. The model uses MODIS data to retrieve the SCA for each pixel. Calibration areas are used to get training data for both snow free areas and areas with full snow cover as shown in the bottom of figure 5.1. The training data is used to make a linearization between the two mean values as we see in the top of figure 5.1.

5.1.1 Cloud detection

Clouds has been a problem in the optical algorithm. We do not want clouds to be detected as snow covered area. Norwegian Computing Center (NR) has experimented on detecting clouds. An algorithm based on K Nearest Neighbour (KNN) is currently the best cloud detection algorithm. The algorithm uses training data from a set of partially cloudy images from a melting season. The KNN uses a multidimensional space $\Re^n$, where n is the number of bands, and computes the distance from the pixel value to all training values. The pixel is classified to the class which is most common among the K closest training data values in $\Re^n$.

A way to mask out clouds and detect snow is written in [17]. The band 2, 4 and 6 from MODIS is used to determine if snow is present by calculating the Normalized Difference Snow Index (NDSI) defined as

$$NDSI = \frac{r_4 - r_6}{r_4 + r_6}, \tag{5.1}$$

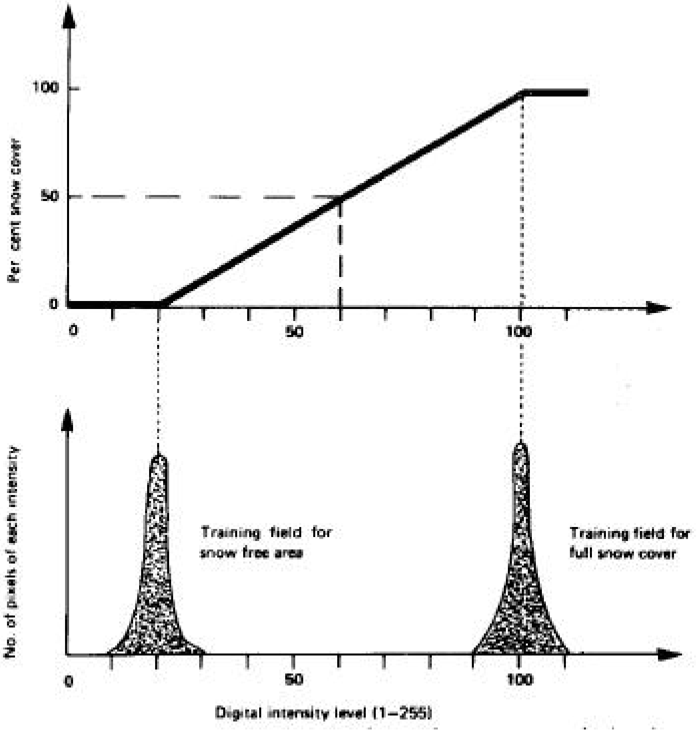

Figure 5.1: Top: The Norwegian Linear Reflectance-to-Snow-Cover (NLR) algorithm. The intensity level in the pixel is lineary transformed to a snow covered percentage for the pixel. Bottom: The training data for both snow free area and full snow covered area. Figure borrowed from [20]

.

where r_i is the reflectance in band i. In areas with no dense forest, the criterion for snow cover is

$$NDSI \geq 0,4 \quad \text{AND} \quad r_2 \geq 0,11 \quad \text{AND} \quad r_4 \geq 0,10. \tag{5.2}$$

The threshold in band 2 and 4 helps to eliminate other areas which can show high values of NDSI such as water [17].

5.1.2 From satellite image to snow cover map

The algorithm used to retrieve snow cover maps from the MODIS measurements are shown in figure 5.2. The image downloaded is a Level 1 product from KSAT. The downloaded data is converted to an internal format, and the cloud detected is performed as descriebed above. The image is then geocoded using the image product. Training data for both snow free and snow covered area are extracted

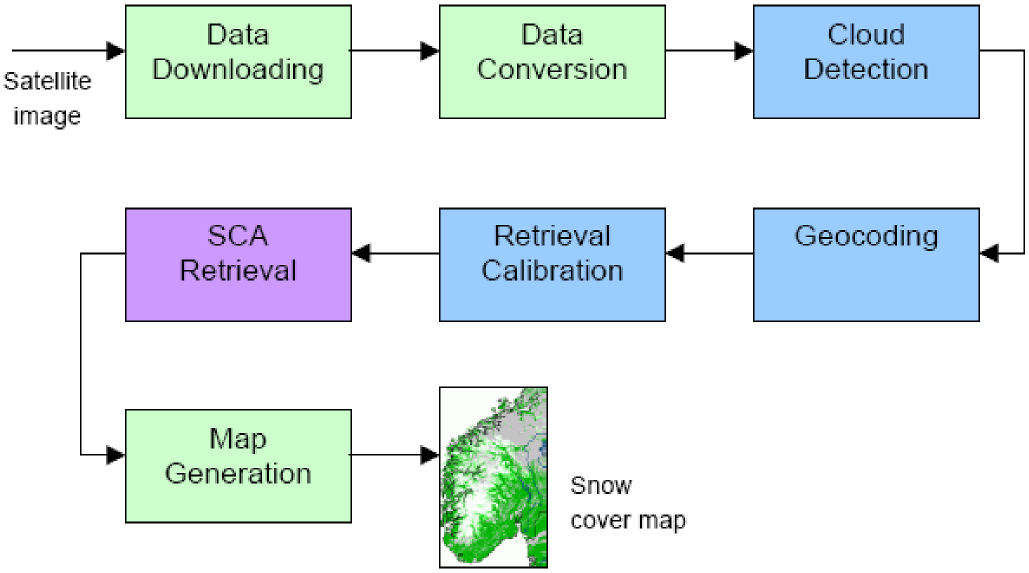

Figure 5.2: Snow cover algorithm for optical data. Figure borrowed from [20]
.

for the image. When the training data is extracted for the image we want to classify we do not need to correct for atmospheric effects, since this will remain constant for the hole scene. Pixel values statistics is calculated for each area, and this statistics are used to detect remaining clouds if there are any, or snow in the snow-free calibration areas. Areas with clouds and areas with snow in the snow-free calibration area are discarted. The accepted calibration areas are used to determine the intensity level for the bare ground and the full snow cover as we see in the bottom of figure 5.1. The snow covered area fraction is now a linear relationship between the intensity level and the two training datas. The SCA is retrieved based on the intensity level, and the result from this is transformed to a raster product with metadata and stored.

5.2 SAR algorithm

The basis of the classification of snow maps is the low backscattering coeffisient (σ^o) of melting snow. A reference image made from images taken when the ground is free of snow, or when it is covered with dry snow is needed. The difference between the σ^o in the melting season compared to the reference images is a clear indication of melting snow [14]. The images are made in two steps. The first step finds the wet snow, while the second step predicts dry snow based on where we finds wet snow.

5.2.1 Wet snow cover algorithm

To get a map over wet snow a good reference image is needed. The reference image should not consist of data from only one scene because of temporal variations in the backscattering, speckle and noise. The amount of moisture in the top layer soil affects the backscattering in a high degree. A reference image that is made by averaging several images will reduce this problem, and also reduce the problem related to speckle [14].

In Norway we can have climate and weather condition that can make it difficult to find a single reference scene that is working well over the whole area we want to make a reference image for. The melting seasons starts in early spring, and can last until the beginning of the autumn. The result is that the reference images have to be obtained between late autumn and mid winter. To be sure that there is none wet snow in the reference image, a mask has been made using temperature measurements in the area and a Digital Elevation Model (DEM). The DEM and a constant lapse rate of 6^{o}C/km were used to interpolate the surface air temperature between the weather stations. Only the weather stations within a 70 km radius were used, and the temperature was then calculated based on the distance from each weather station. In this way, the areas with temperature above the freezing point were masked out since it likely contained wet snow [21]. In the end, the reference image is made by averaging all unmasked measurements in each pixel. The reference image should have the same spatial resolution as the image we want to check for wet snow.

The image we want to run through the algorithm (the snow image) is first geocoded so each pixel in the snow image will be compared to the same pixel in the reference image. The ratio between the backscattering coefficient of the snow image (σ^{o}_{ws}) and the reference image (σ^{o}_{ref}) is then calculated pixel by pixel. The DEM and information about the orbit and image paramteres are then used to calculate a map with radar shadow (RS), and a map of local incidence angle. Also a land mask (LM) with information about the land is used to mask out sea and lakes. The next step is to use the backscatter ratio ($\sigma^{o}_{ws}/\sigma^{o}_{ref}$) to make a map over wet snow. This is done by setting a threshold for the ratio, and a binary snow map is made by the following algorithm:

```
if ($RS$ = TRUE or $LM$ = TRUE) then snow mapping not possible
else if ($\sigma^{o}_{ws}/\sigma^{o}_{ref} < TR$) then wet snow
else then snow free or dry snow
```

Nagler and Rott [14] found that $\sigma^{o}_{ws}/\sigma^{o}_{ref}$ was typically -5 to -7 dB for wet snow

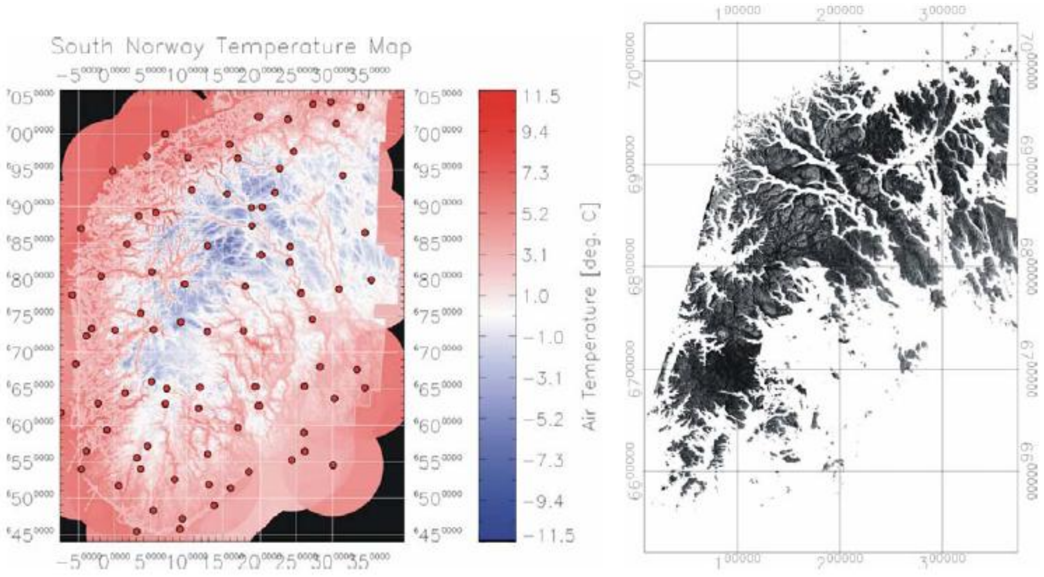

Figure 5.3: Left: The dots represents all weather stations in South Norway. The map is a temperature field map made by interpolating the measurements from the weather stations with a 100 × 100 meter resolution DEM and a constant lapse rate of 6^oC/km. The map is for March 10, 2003 at 10am. Right: SAR backscatter reference image covering a small part of South Norway. The image is taken the same day, and the pixels with temperature over the freezing point is masked out. Illustration borrowed from [21].

areas and +2 to 0 dB for snow free areas. The threshold was therefore set to TR = -3 dB.

5.2.2 Dry snow cover algorithm

Since the backscatter coeffisient of the dry snow is approximately the same as the backscatter coeffisient for bare ground $\sigma_{ds}^{o} \approx sigma_{ref}^{o}$, it is not possible to derive dry snow directly from the backscatter intensity difference between the ASAR scene and the reference scene. We can however make a map over dry snow by calculating the probablility of dry snow based on the wet snow cover map, temperature in the area and the DEM. Our algorithm is a refinement of the method suggested in [12] and prescribes snow in areas fulfilling the following requirements:

1. the altitude of the pixel is above the mean altitude of the identified wet snow pixels within a sliding 20 × 20 km^2 box centered at the pixel;

2. at least 2% of the pixels in the sliding box must contain wet snow;

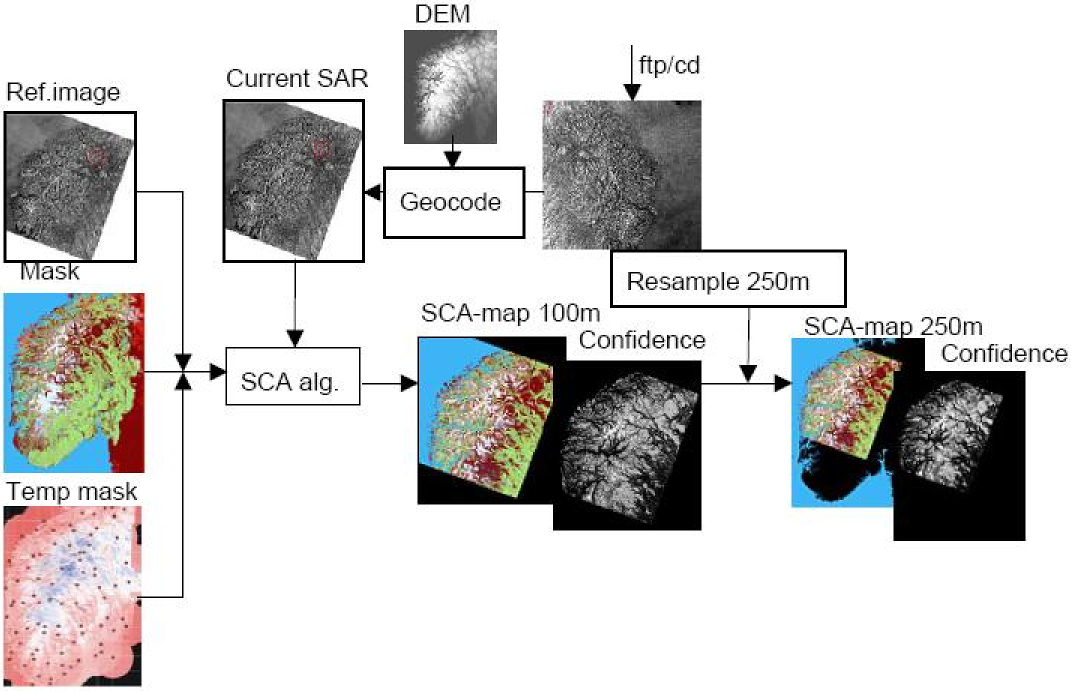

Figure 5.4: Diagram showing the steps involved in produsing the SCA maps from repeat pass ASAR wideswath data. Illustration borrowed from [21].

3. the temperature in the air in the pixel is below the freezing point.

The last two points prevent erroneous calculation of dry snow at higher elevations late in the season [21].

To be able to use these images more easily we need a resolution of 250 × 250 meters instead of 100 × 100 meters. This is easily done by resampling the image.

5.2.3 Confidence flags

Confidence flag maps are made in addition to the snow covered area-maps and reference image. This flag is the probability of classifying the pixel correct. The confidence flag map of the reference image are based on the air temperature. Since the algorithm for detecting SCA are based on probability, some pixels have a higher probability of being classified correct than others. The confidence flag maps contain an estimate of this percentage probability. The confidence are calculated differently for the pixels with wet and dry snow. For wet snow, the satellite geometry, the confidence value of the reference image and the difference between threshold value decide the confidence value. The elevation difference between the wet snow mean altitude and the air temperature contribute in addition to these for calculating the confidence of dry snow [15].

5.2.4 Problems with the SAR algoritm

There are several problems with this SAR algorithm. The biggest problem is probably the prediction of dry snow. One problem with this algorithm is that it is necessary to have wet snow in the area to predict the dry snow. This problem is hence larger early in the melting season.

An example of this error can be seen in figure 5.5. The mean temperature in Røros on the 4th of April 2008 was $3,6^o$C with a maxima of $8,9^o$C. There was no registred precipitation at Røros Aiport between the 22nd of March and 4th of April 2007 [23]. The days before the 4th of April 2007 it was colder, so most of the snow was dry on the 4th at noon when the image was taken. Because of the temperature the day before, more snow had become wet on the 5th, and the SAR algorithm detected much higher snow covered area (SCA). If we compare the resulting SCA from the MODIS measurement in the bottom left in figure 5.5 and the resulting SCA from the ASAR measurement in the upper left, we can see a big difference even though some of the area on the MODIS measurement are covered with clouds.

Changes in surface roughness and wetness can also create temporal changes of σ^o and therefore problems with the classification algorithm over e.g. agricultural surfaces and wetlands.

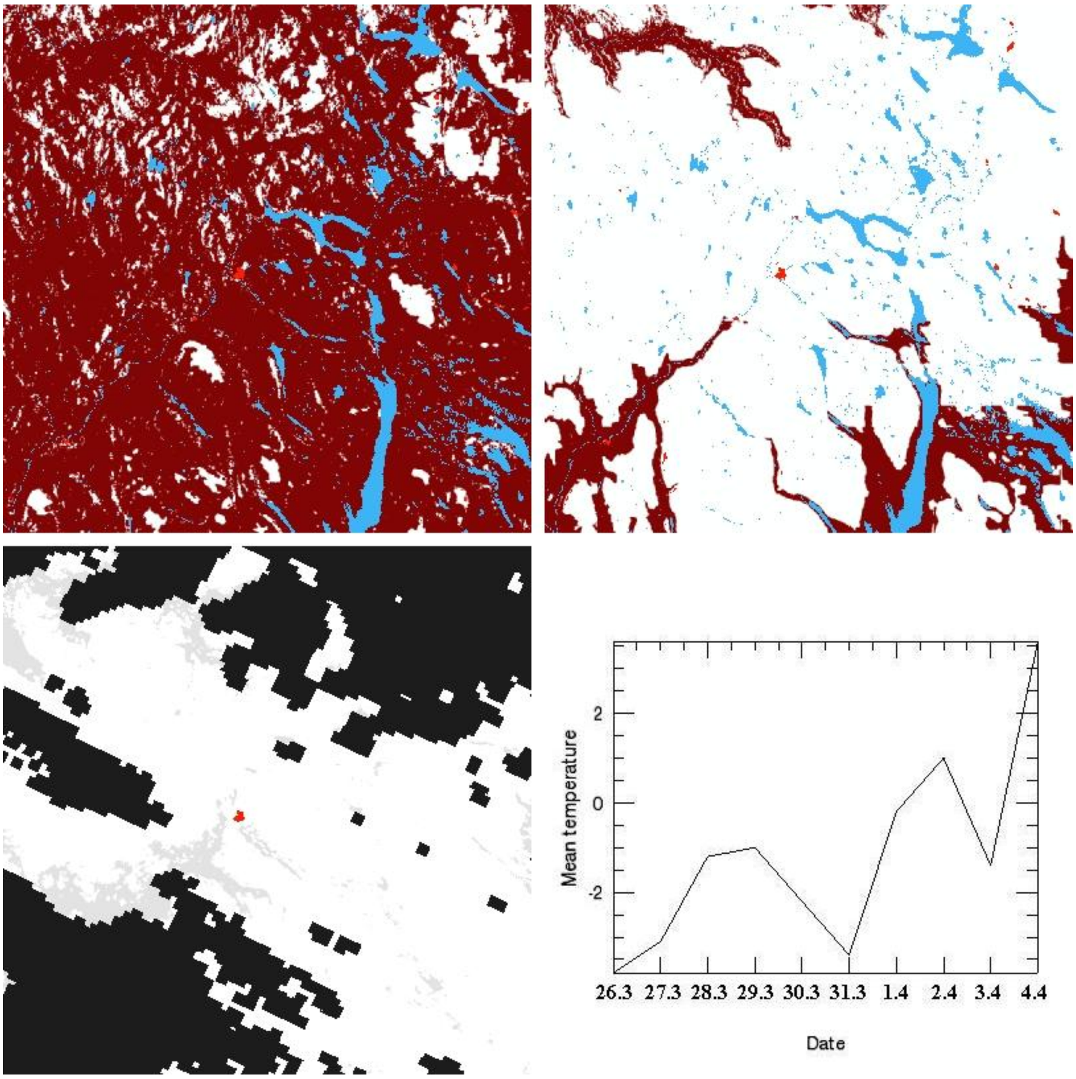

Figure 5.5: Upper left: ASAR image after running through the algorithm. The image is from the area around Røros taken on the 4th of April 2007. White colour represents SCA while dark red is bare ground and blue is lakes. The brighter red spot in the middle is the centre of Røros. Upper right: ASAR image run through the algorithm, from the same location taken on the 5th of April 2007. Bottom left: MODIS image from the same area on the 4th of April 2007. White colour represents SCA, while black is no information (clouds). Bottom right: Mean temperature at Røros Airport the days before the images was taken.

Chapter 6

Other input data

In addition to the SCA-measurements we will use some additional information about the environment.

6.1 Land cover masks

The land cover masks contain information on what kind of land cover the pixel contain. We use two different masks, and both have the same spatial resolution as the MODIS measurements, 250m. The first mask is only used to mask out pixels which needed needed to be treated differently. As we see from table 6.1 these are sea, lakes and glaciers.

The second land cover mask contain more detailed information about what kind of land cover and vegetation is present. The map was made from a total of 45 Landsat TM/ETM+ images with a ground resolution of 30 × 30 meters. The images were processed in six operational stages; spectral classification, spectral similarity analysis, generation of classified image mosaics, ancillary data analysis, contextual correstion and standardization of the final map products. The map has a total of 35 different classes plus one for unclassified land cover, as we can see in table 6.2. The map was later interpolated to get a 250 × 250 meter resolution [9].

Table 6.1: Overview over values for different content in the first mask.

Value	Type
20	Sea
21	Lake
70	Glacier
0	Other

Table 6.2: Overview over values for each type of classes in the second mask.

Value	Type of land cover
0	Unclassified
1	Spruce forest
2	Coniferous forest - dense canopy layer
3	Coniferous forest - matured danopy layer
4	Coniferous forest - open canopy layer
5	Pine forest
6	Open pine forest
7	Lichen birch woodland
8	Mountain birch forest
9	Empetrum birch forest
10	Bilberry birch forest
11	Tall herb forest
12	Low herb forest
13	Hummock bogs
14	Lawn and carpet mire complex
15	Tall sedge fen
16	Wooded mire complex
17	Mud-bottom fens and sedge marches
18	Exposed ridges - scarcely vegetated
19	Open heather communities
20	Heather communities
21	Lichen heaths
22	Dwarf shrub heaths
23	Fresh heaths and grey-willow thickets
24	Grass heaths
25	Tall herb meadows
26	Low herb meadows
27	Moderate snowbed communities
28	Snowbeds
29	Mid-alpine ridge communities
30	Bare rocks and high-mountain gravel fields
31	Snow and glaciers
32	Water
33	Cultivated areas
34	Town, cities
35	Impediment

Table 6.3: Overview over the scale for SCA from weather stations.

Scale	Meaning	Our interpretation
0	No snow	0%
1	Mostly snow free, but some snow spots	25%
2	About 50% snow cover	50%
3	Mainly snow, some free spots	75%
4	100% snow cover	100%

Table 6.4: Overview over the weather stations used.

Name	Elevation	Location (UTM 33)	Pixel
Oppdal - Sæter	604 metres	312611(E) 6943791(N)	(1210,3956)
Røros Airport	625 metres	226441(E) 6952817(N)	(1554,3993)
Tingvoll - Hanem	69 metres	159145(E) 6985586(N)	(941,3825)

6.2 Meteorological measurements

To be able to check the results we get, it is nice to have something to compare the results with. The Norwegian Meteorological Institute has a lot of measurements open for everyone online, so we got our information from them. The information we are after are temperature, snow depth and precipitation. We also get information about the snow cover, but there is a big uncertainty of how accurate this number is. The snow cover data had a scale from 0-4 as we can see in table 6.3. These observations are based on the snow cover 1 km around the weather stations [23].

We selected three weather stations based on location, elevation, and climate. One of them is at low elevation by the sea (Tingvoll - Hanem), one in a valley (Oppdal - Sæter) and the last one on a gently sloping plateau with a cold climate (Røros Lufthavn). Information about these stations can be found in table 6.4.

6.3 Digital Elevation Model (DEM)

A Digital Elevation Model (DEM) is a digital representation of the elevation. It will be used to compare the snow covered area with the elevation. Our DEM is made by Statens kartverk and had originally a resolution of 25 × 25 meters. The DEM is based on contour curves, terrain points, water from N50 maps and also roads from Vbase (a digital road database for Norway) [27]. The original DEM is interpolated to get new DEMs with resolution of 100 × 100 and 250 × 250 meters to fit our data. The DEM with resolution of 100 × 100 is used in the calculation of the probability of dry snow in the ASAR algorithm.

Chapter 7

Methods for calculating snow covered area

In this chapter we will explain the methods we use in our experiments. There are several possible ways to think about this problem. One way we will look into is hindcasting of the snow covered area, to be able to fill in data where we have no measurements. Another way we will look into is nowcasting, where we try to predict the current snow covered area based on the past and current measurements. A third method is forecasting, but we will not look into this in this thesis. Forecasting of snow covered area is difficult since we would need to predict snow fall too.

Figure 7.1 is showing the measurements for one pixel. As we see, there are many days without measurements (e.g. day 111-114 and 146-149). On day 110 a MODIS-measurement of 100% snow covered area (SCA) was done, but five days later a ASAR-measurement of 0% SCA was done. What was happening in between these measurements is a problem we will look more into.

7.0.1 Hindcasting

If we only want to hindcast past data, we will need to fill in data for the days with no measurements, and a simple interpolation can be used. The data on the missing days will then be dependent on both past and future measurements. A problem with this kind of approach is what happens in practice. Snow usually do not cover a bigger area little by little over several days. The snow covered area usuelly get bigger very suddenly when it is snowing. Also the melting does not happen in a linear way. The SCA usually decreases faster in the middle of the melting period than in the beginning and in the end, since peaks melts very early, while some piles of snow may stay for a long while. The result is that this approach can give output that changes before the change actually happened. This approach

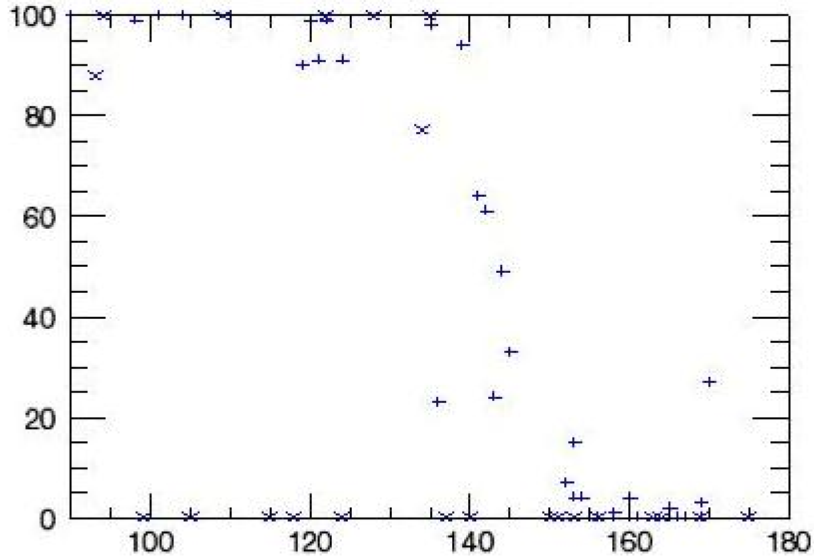

Figure 7.1: Measurements for one pixel, 17 km north east of the centre of Oppdal at 918 meters above sea level, made from data from spring of 2007. The pixels location is the third x from the left in figure 7.2. The pluses is measurements done by MODIS, while the x'es is measurements done by ASAR. The x-axis denotes the day after new year 2007, while de y-axis is percentage snow covered area.

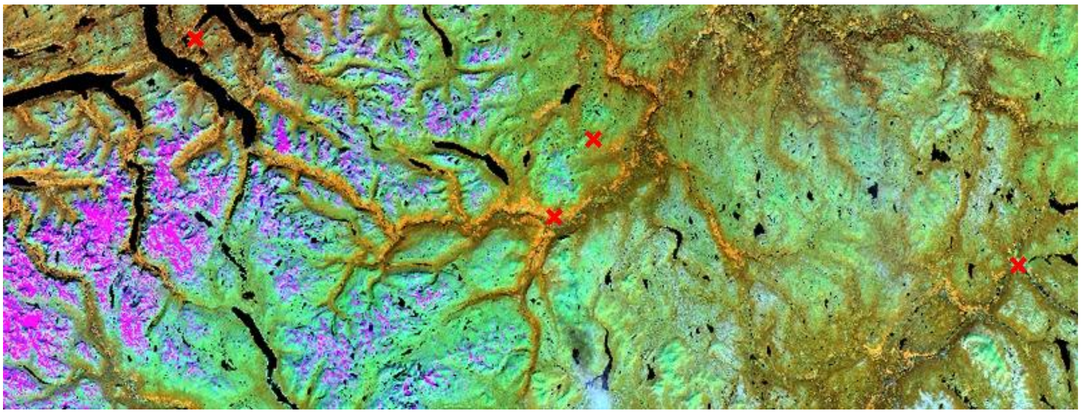

Figure 7.2: Image taken over the area we are looking at. The four red x'es represents interesting areas. The x'es represents (from left to right) the weather station at Tingvoll - Hanem, the weather station in Oppdal - Sæter, the location of the pixel used in several figures, such as 7.1 and the last x represents the weather station at Røros Airport. The image is taken by Landsat, and the bands used are 4 (near infrared), 5 (middle infrared) and 3 (red). The colours are false.

will work well for filling in data from missing days for past data set.

An example of filling in missing data is described in section 7.2, but we will also test the performance of the Kalman filter in section 7.3 for this purpose.

7.0.2 Nowcasting

Another approach in snow cover estimation is to always try to predict the present SCA based on both past and current data. If we know how high the snow covered area was in the past days, we should be able to predict the snow melt for the next days as well. The problem areas is the areas not covered by the new image because of clouds etc. These areas needs to be predicted based on past data only, which can be a problem. Present or future snow fall can never be predicted based on past SCA-maps only, and since this approach only is based on past SCA-measurements, "expected" changes will only change the output when a new measurement implies that this change has happened. This approach should work well if we have real time data, and we want to find out what the snow covered area is at present.

This approach to the problem will be described better in section 7.3.

7.1 Main Algorithm

In figure 7.3 we can see the flowchart from the main algorithm. The algorithm can be explained point by point:

1. The algorithm starts by reading the mask which contained the information over sea, lakes and glaciers.

2. The value of the line number l is set. Together with the sample m it gives a coordinate to each pixel.

3. The measured SCA is read from the files, but only line l from every data file. The reason for this is that if all lines are read, the SCA-array will contain about 10 billion values, or allocate about 10 GB of memory, and the algorithm will be slow since the computer we use typically have 2 GB available memory. Virtual memory using the harddisk as swap-space makes the process run very slowly. Instead it read only one line from each image file, and the memory use is down to 1,5 MB.

4. The value of the sample number m is set.

5. The algorithm test what value the mask has in pixel (m,l). The test has four possible outcome.

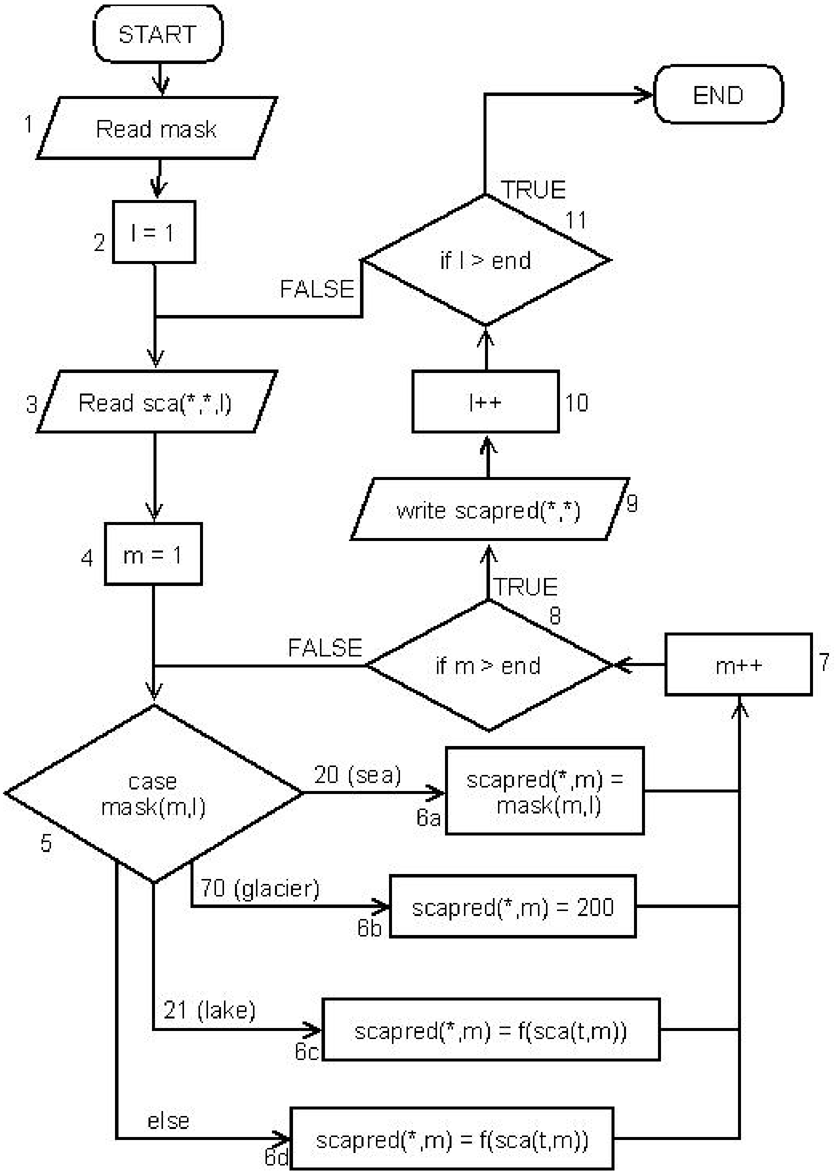

Figure 7.3: Flowchart over the algorithm used to calculate snow covered area.

6. The value of the mask can be;

    - a) 20 - The pixel is in the sea, and the output is set to 20;
    - b) 70 - The pixel is in a glacier, and the output is set to 200;
    - c) 21 - The pixel is in a lake, and a filter predicts the lake ice status;
    - d) else - The pixel is in any other land cover, and a filter predicts the SCA.

Table 7.1: Overview over possible values for the predicted SCA.

Value	Type
20	Sea
21	Lake
255	Ice on lake
100-200	0-100% SCA
30	No information

We will explain more about the filters we use later in this chapter. The outcome of the predicted SCA from the filters is listed in table 7.1. As we see, the values for sea and lake are the same as the mask used.

7. The sample number m is updated.
8. A test check if it is at the end of the current line. If we are not at the end of the line, the algorthm will go back to point 5. If we are at the end of the line, the algorithm will continue to point 9.
9. The predicted SCA is written to the files, one file for every day (t), but a different temporal resolution could also be used of desirable.
10. The line l is updated.
11. The algorithm checks if we are on the last line. If not, it will go back to point 3 and starts all over with the next line. If we are on the last line, the algorithm terminates.

7.2 Moving average filtering

The easiest method we have looked into for filtering the data is simply smoothing the data with a moving average filter, and then interpolate the result from the smoothing. This is a method that fill in missing data, and the output will be dependent on both past, current and future measurements as we see in the equation for the moving average filter;

$$x(k) = \frac{1}{\omega} \sum_{j=k-\frac{\omega-1}{2}}^{k+\frac{\omega-1}{2}} y(j), \tag{7.1}$$

where y is the measurements and ω is how many measurements we want to smooth. We have used a window of size 5, which mean that $x(k)$ will be the average of the two past, the current and the two next measurements. The result from the moving average filter $x(k)$ is then interpolated into $\hat{x}(t)$, where k is the time of the measurements, while t is the time every day at noon (12 p.m.). The interpolation is done by using the least squares quadratic fitting method. The method use the 4 neighbours x_{k-1}, x_k, x_{k+1} and x_{k+2}, where $k \leq t < k+1$, to find the best fit to the equation $z = a + bx + cx^2$. The curve is found by minimizing

$$R^2 = \sum_{i=k-1}^{k+2} [x_i - z]^2. \tag{7.2}$$

The moving average filtering method has been used mainly to show the difference between a simple filter where every measurement count equally and the result from our Kalman filter, which tend to put more weight on the current measurement, at least for SCA-data with relative high signal noise.

7.3 Kalman filtering

In chapter 4 we explained the theory behind the simple and the extended Kalman filter. The Kalman filter we use is an extended Kalman filter. It uses only the past and the current measurements to calculate the current SCA-maps. We also want to make it possible to predict current snow covered area where we have no current measurements, and the Kalman filter is a good choice for this purpose.

The state $x \in \Re$ the Kalman filter will try to predict is the snow covered area (SCA). The model we use for $x(t)$ is a sigmoid. The reason for this is our experience from the typical temporal development of snow covers. The equation for $x(t)$ can be written as

$$x(t) = 100 - \frac{100}{1 + e^{-\beta(t-T_0)}}, \tag{7.3}$$

which also can be written as

$$x(t) = \frac{100e^{-\beta(t-T_0)}}{1 + e^{-\beta(t-T_0)}}. \tag{7.4}$$

The measurement $z \in \Re$ is described as

$$z(t) = h(x(t), v(t)). \tag{7.5}$$

The h for MODIS and ASAR measurements are assumed to be linear and equal to 1, so we get

$$z(t) = x(t) + v(t), \tag{7.6}$$

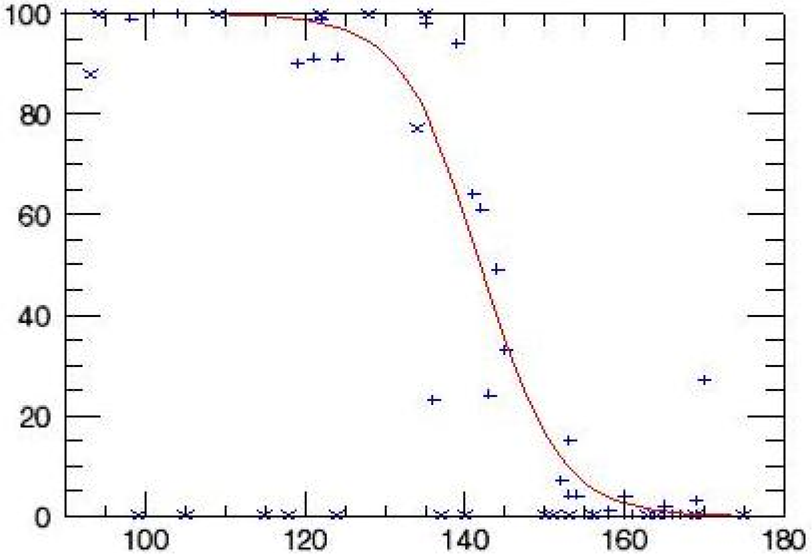

Figure 7.4: Example of the measured snow covered area for a pixel. The pluses are measurements done by MODIS, the x'es are measurements done by ASAR and the red line is the best fit for equation 7.3 for the MODIS-measurements. This pixel is the same as figure 7.1.

where $v(t)$ is the measurement noise. As we see this is much simpler than the extended Kalman filter described in chapter 4.

β and T_0 are derived by finding the minimum mean squared error (MMSE) for each year 2003 to 2007. The MMSE was found by minimizing the mean squared error (MSE), which is given by

$$MSE(x(\beta, T_0)) = (y(t) - x(t, \beta, T_0))^2, \tag{7.7}$$

where $y(t)$ is the actual measurement and $x(t, \beta, T_0)$ is the equation 7.3 at the time of the measurements $y(t)$. The result of this is five curves $x_{2003}(t)$, $x_{2004}(t)$, $x_{2005}(t)$, $x_{2006}(t)$ and $x_{2007}(t)$ that fits our measurements best. We only use MODIS measurements for this, since they give better information about the exact SCA. The important thing here is to find the curve from the whole melting season, and the MODIS measurements are much better at this than the ASAR. We find one value for β and T_0 for every pixel and every year from 2003 until 2007 where we have a minimum of 5 MODIS measurements in the melting season. We are interested in the mean curve $x_{mean}(t)$ from these 5 years, which is given by

$$x_{mean}(t) = \sum_{i=2003}^{2007} \frac{x_i(t)}{5} \tag{7.8}$$

Since we want a curve that is given by the parameters β and T_0 only, like in equation 7.3, we need to minimize the MSE of $x_{mean}(t)$;

$$MSE(x(\beta, T_0)) = (x_{mean}(t) - x(t, \beta, T_0))^2, \tag{7.9}$$

which will give us an approximate curve $\hat{x}_{mean}(t)$ for the mean SCA as a function of time with a resulting β_{mean} and $T_{0_{mean}}$.

We have now 6 values of both β and T_0. 5 of them are the values for each year, and one mean value. If we run the measurements from 2007 through the filter, we will of course get a better result when using β_{2007} and $T_{0_{2007}}$ than e.g. β_{2003} and $T_{0_{2003}}$. But if we choose to run the measurements from 2008 though the filter we have no β and T_0 which are calibrated for this year. The soultiuon we choose for this is to check which of the curves $x_{2003}(t)$, $x_{2004}(t)$, $x_{2005}(t)$, $x_{2006}(t)$, $x_{2007}(t)$ and $x_{mean}(t)$ fits our measurements best. The equation for this is the same as equation 7.7, where $x(t, \beta, T_0)$ is $x_{2003}(t)$, $x_{2004}(t)$ etc.

To find the value $x(t+\Delta t)$ we have to differenciate $x(t)$. If we take the derivative of equation 7.3 we get

$$\frac{dx}{dt} = \frac{-100\beta e^{-\beta(t-T_0)}}{(1+e^{-\beta(t-T_0)})^2}, \tag{7.10}$$

which we can write as

$$\frac{dx}{dt} = \frac{100^2 e^{-2\beta(t-T_0)}}{(1+e^{-\beta(t-T_0)})^2} \frac{-\beta}{100} e^{\beta(t-T_0)}. \tag{7.11}$$

This is the same as

$$\frac{dx}{dt} = -x(t)^2 \frac{\beta}{100} e^{\beta(t-T_0)}, \text{or} \tag{7.12}$$

$$\frac{\Delta x}{\Delta t} = -x(t)^2 \frac{\beta}{100} e^{\beta(t-T_0)}. \tag{7.13}$$

It is now easy to calculate $x(t+\Delta t)$ as

$$\begin{aligned} x(t+\Delta t) &= x(t) + \Delta x \Delta t \\ &= x(t) - x(t)^2 \frac{\beta}{100} e^{\beta(t-T_0)} \Delta t. \end{aligned} \tag{7.14}$$

Since we typically are choosing $\Delta t = 1$ we get

$$x(t+\Delta t) = x(t) - x(t)^2 \frac{\beta}{100} e^{\beta(t-T_0)}. \tag{7.15}$$

To get this on the same form as equation 4.35 we may write this as

$$\begin{aligned} \hat{x}_k^- &= f(\hat{x}_{k-1}, u_{k-1}, w) \\ &= \hat{x}_{k-1} - \hat{x}_{k-1}^2 \frac{\beta}{100} e^{\beta(t_{k-1}-T_0)} \end{aligned} \tag{7.16}$$

where $\hat{x}_k^-$ is the a priori state estimate, while $\hat{x}_k$ is the a posteriori state estimate. We are not using any control-input in our Kalman filter, so $u_k = 0$. The process noise w and the measurement noise $v(t)$ are both white Gaussian noise with probability distributions

$$\begin{aligned} p(w) &\sim N(0, Q), \text{and} \\ p(v(t)) &\sim N(0, R(t)), \end{aligned} \tag{7.17}$$

where Q is the process noise variance and $R(t)$ is the measurement noise variance. Note that the process noise is constant.

To calculate the relation between the past step and the current step $A \in \Re$, we need to look at equation 4.2. To calculate A we use this equation

$$\begin{aligned} A &= \frac{\partial f(\hat{x}_{k-1}, 0, 0)}{\partial x} \\ &= \frac{\partial (\hat{x}_{k-1} - \hat{x}_{k-1}^2 \frac{\beta}{100} e^{\beta(t_{k-1} - T_0)})}{\partial x} \\ &= 1 - 2\hat{x}_{k-1} \frac{\beta}{100} e^{\beta(t_{k-1} - T_0)} \end{aligned} \tag{7.18}$$

7.3.1 Time update (”predict”)

The time update of our extended Kalman filter is simpler than the extended Kalman filter explained in the theory part. But in our filter, the time update is done once every day independently if there are a measurement this day or not. The equations for the time update is

$$\hat{x}_k^- = \hat{x}_{k-1} - \hat{x}_{k-1}^2 \frac{\beta}{100} e^{\beta(t_{k-1} - T_0)}, \text{and} \tag{7.19}$$

$$P_k^- = A_k^2 P_{k-1} + Q. \tag{7.20}$$

The process noise was set to $Q = 0.07^2$ since it seemes to fit the model. β and T_0 in equation 7.19 is selected as the minimum mean squared error from the six possible variables described earlier. β and T_0 does not vary with each step, but are decided in the beginning depending on the MODIS measurements. The time t_{k-1} in equation 7.19 has to be calculated using equation 7.3;

$$t_{k-1} = -\frac{log(\frac{100}{100 - \hat{x}_{k-1}} - 1)}{\beta} + T_0 \tag{7.21}$$

The predicted SCA is based on the SCA the day before. In this way we always predict the snow to melt based on how far the melting has gone, and not on what date it is. When we look closer at equation 7.21 we see that if $\hat{x}_{k-1} = 100$, t_{k-1} will not get a value, since $log(\infty)$ is not possible to calculate. Because of this we have choosen to force the algorithm by putting on a test that set $\hat{x}_k = 100$ if $\hat{x}_k > 95$ and $\hat{x}_k = 0$ if $\hat{x}_k < 5$.

7.3.2 Measurement update (”correct”)

The time is updated every day, and this creates a problem in the measurement update. There are two possibilities how the measurement update is handled.

No measurement

If there are no measurement this day we use these formulas;

$$\hat{x}_k = \hat{x}_k^-, \text{and} \tag{7.22}$$

$$P_k = P_k^-. \tag{7.23}$$

Equation 7.22 set the a posteriori state equal the a priori estimated state, and equation 7.23 set the a posteriori estimate error variance equal to the a priori estimate error variance. As long as there is no measurement for some days, the cyclus would cycle between the time update and the no measurement-measurement update, and the estimate error variance will get higher and higher, since A in equation 7.21 is close to 1.

One or more measurements

The days there are measurements the equations we use are these;

$$K_k = \frac{P_k^-}{P_k^- + R'} \tag{7.24}$$

$$P_k = (1 - K_k)P_k^- \tag{7.25}$$

$$\hat{x}_k = \hat{x}_k^- + K_k(z' + \hat{x}_k^-). \tag{7.26}$$

The measurement error variance R' in equation 7.24 is depended on how many measurements it is that day, and with what instrument. The equation for calculating R' is

$$\begin{aligned} \frac{1}{R'} &= \frac{1}{R_1} + \frac{1}{R_2} + \cdots + \frac{1}{R_n}, \\ R' &= \frac{1}{\sum_{i=1}^{n} \frac{1}{R_i}} \end{aligned} \tag{7.27}$$

where n is the number of measurements this day. To calculate the measurement error variance R_i of a measurement we use this equation;

$$R_i = (S_i \times \frac{250 - 2 * R_m}{1000})^2, \tag{7.28}$$

where $S_i = 1$ if the measurement is done by MODIS and $S_i = 2$ if the measurement is done by SAR. $R_m \in [0, 100]$ is the calculated confidence from the confidence flag-input. Equation 7.28 is chosen because it fits our purpose well. The measurement error variance is higher when the value from the confidence flag is low, and the error variance is smaller for MODIS-measurements than for ASAR-measurements.

The measurement z' we use in equation 7.26 does also need some extra calcultaions if there are more than one measurement this day. The equation for z' is

$$\begin{aligned} z' &= \frac{\sum_{i=1}^{n} \frac{z_i}{R_i}}{\sum_{i=1}^{n} \frac{1}{R_i}} \\ &= \sum_{i=1}^{n} \frac{z_i}{R_i} R' \end{aligned} \tag{7.29}$$

Equation 7.29 emphasize the measurements with low measurement error variance by taking a weighted mean of all measurements where the variances of the other measurements are the weights.

If there are none measurements for some days, the estimate error variance will be high, and the new measurement will be emphasized.

7.3.3 Initial settings

We need some initial settings for our Kalman filter as we saw in the example in section 4.3. The initial state estimate $\hat{x}_0$ is the estimated snow covered area on January 1, and we estimate this to be $\hat{x}_0 = 100\%$. Even if this is wrong, it is not that important, since the values we are after is the melting season, which starts later. We assume the process variance is small $Q = 0,005$.

The initial value of the estimate variance P_0 is harder to estimate. In the example in section 4.3 P_k converged to one value, but our x_k and R_k changes for every step k, so P_k will not converge. But as we have said earlier, the value P_0 is not that important. We have therefore choosen to set $P_0 = 0$. Since we have set $Q = 0,005$, the process will not believe $\hat{x}_k \approx \hat{x}_0 = 100$, and P_k will change for every step k. In the example in section 4.3 we saw that P_k converged after about 30 steps, and since we are only after what happens from April 1 (day 90), we assume P_k will have its "correct" estimate variance by then. This is assumed that we have measurements earlier than April 1, something we do not have with MODIS. But we have measurements for ASAR earlier than April 1, so the assumtion are not incorrect.

Chapter 8

Results

8.1 Introduction

In this chapter we will perform ”experiments” where we study the temporal and spatial development of SCA by using the methodology developed in chapter 7. We will also explain the results from these ”experiments”. We have analyzed the existing data using two filters, a moving average filter and an extended Kalman filter, and we will give some examples on the results they gave us. We will further discuss these results, and compare the two filters. We will also look at the results and compare them with the vegetation map from section 6.1 and the digital elevation model (DEM) in section 6.3.

The area we have looked into is an area about 75 × 200 km in the middle of Norway. The area streches from Åndalsnes in the west, Soknedal in the north, Tynset in the south and about 10 km east of Røros. This area was selected because of its variety in topography and climate.

8.2 Moving average filtering

The moving average filter fills in the missing data, and figure 8.1 show us a result from this. The measurements are taken from the same location as figure 7.1 in 2007. All MODIS measurements until day 136 (May 17, 2007) indicate that the snow covered area (SCA) was at least 90% before day 136. The ASAR-measurements are divided into 5 measurements at 100% and 2 measurements close between 75 and 90%, and 5 measurements at 0%. This is a clear indication that the ASAR-measurements are not as reliable as the MODIS-measurements. But the moving average filter is weighting the measurements equally no matter what instrument that did the measurements, and the result is what we can see in figure 8.1. The filter estimating the SCA too low, as low as 50% while the SCA probably

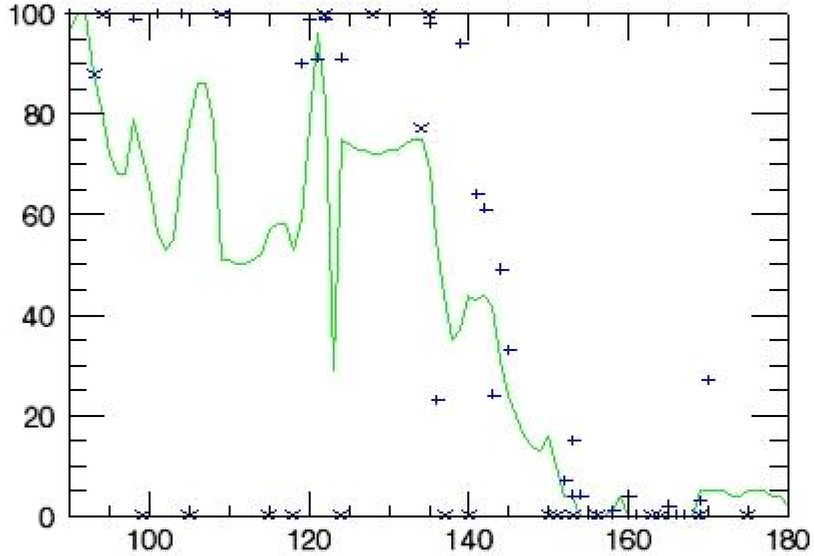

Figure 8.1: Result from using a moving average filter on the MODIS and SAR measurements. The pluses are measurements done by MODIS, the x'es are measurements done by ASAR and green line is the result from the moving average filter. The location of the pixel is the same as in figure 7.1.

was approximately 100% at this time.

The melting seems to start around day 130 (May 11, 2007), and compared to the MODIS-measurements, the estimation seems to show too low SCA all the time, except two measurements. The measurement of 23% SCA at day 136 seems to be errorous since MODIS the day before measured the SCA to be 98%. There were a lot of clouds this day, so this might have disturbed the measurement. A visual inspection of the MODIS data for this day confirms that this can be the issue. Since the pixel is in between other pixels classified as clouds, and the value of a pixel next to it had an estimated SCA-measurement of 92% we can assume the cloud detection algorithm did an errorous classification for this pixel.

8.3 Results from the Kalman filter

In chapter 7 we said we wanted to look into two possible ways to solve this problem. One is hindcasting, or filling in missing data, and the other one is nowcasting, which means to predict current data based on the past and current measurements. Our Kalman filter may do both, although both approches only take old and current measurements into account when estimating the SCA. We will show the results from both these approches and see the difference between them.

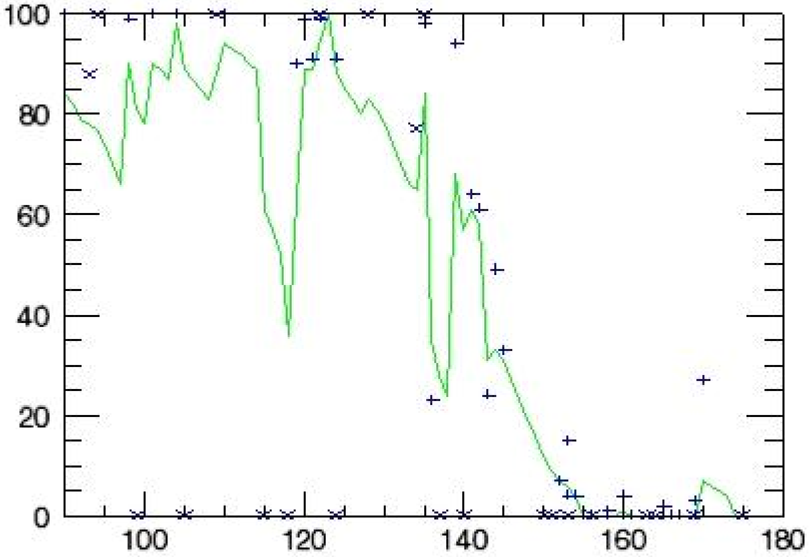

Figure 8.2: Result from using an extended Kalman filter on the MODIS and SAR measurements. The pluses are measurements done by MODIS, the x'es are measurements done by ASAR and green line is the result from the extended Kalman filter using $x_{2007}(t)$. The location of the pixel is the same as in figure 7.1 and 8.1.

8.3.1 Hindcasting

To fill in the missing data using our extended Kalman filter, we have to use the β and T_0 obtained from the same dataset as we will filter. β and T_0 are obtained using equation 7.9. The resulting estimation of the SCA is shown in figure 8.2. This is the same location as in the example from the moving average filter in figure 8.1.

There is a big drop in the estimated SCA around day 115-118 (April 26-29, 2007). As explained before, when there has been no measurements for some days, the next measurement will be weighted heavily. There is a measurement done by MODIS on day 110 (April 21, 2007) with 100% SCA, but after that there were 4 days without a measurement for that area. When ASAR measured 0% SCA on day 115, and later at day 118, these made the estimated SCA drop down to about 35%.

If we compare the result from the extended Kalman filter in figure 8.2 with the result from the moving average filter in figure 8.1, we can see the extended Kalman filter generally predicts a higher snow covered area than the moving average filter, and estimate the SCA to be closer to the MODIS measurements.

Another example of this behaviour of the Kalman filter can bee seen in figure 8.4. Here we are looking towards west in the area around Oppdal. The twelve

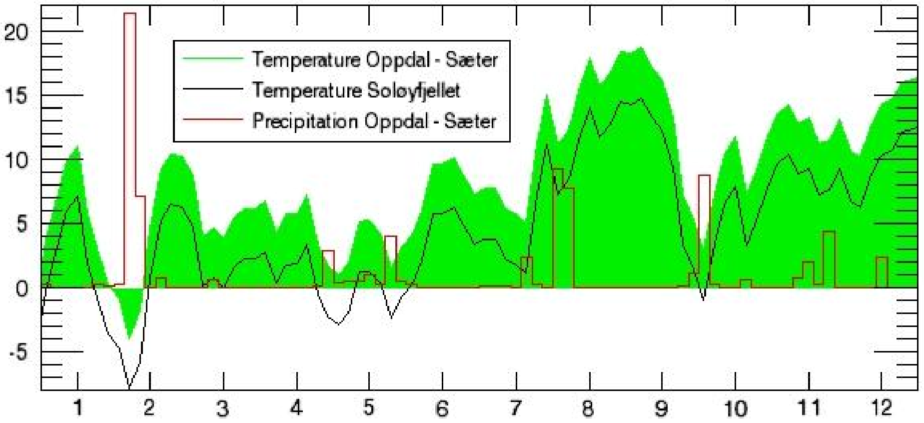

Figure 8.3: Temperature and precipitation for the area in figure 8.4. The temperature in green is the temperature in °C, measured at the meteorological weather station in Oppdal - Sæter. The black line represent the temperature at the plateau in the upper left in the images in figure 8.4. The red histogram represents the precipitation in mm measured at Oppdal - Sæter. The temperature at the plateau is derived from the measurements at the weather station by subtracting the elevation difference multiplied with a lapse rate of 6°C/km. The x-axis denotes the week number in figure 8.4, such that the image taken on April 15, 2007 is at week 1, all the way to July 2, 2007, which is week 12.

images are taken one week apart in the period April 15 until June 4, 2007. Magenta represents snow covered lakes, blue is lakes without snow cover, dark green is bare ground, white is 100% snow cover, while the colours between white and green represents snow covered area between 100% an 0%.

If we take a look at Gjevilvatnet (the lake in the upper right), we can see that it is fully covered with snow until May 21, 2007, but the snow is not gone until the next image on May 28, 2007. Svarthaugen is the name of the small hill in the middle of the valley. It is partially covered with snow until May 7, 2007, when only the top is partially covered. All snow from the top is not gone until May 28, 2007. It is also easy to see that the snow is melting earlier in the valley than on the mountains.

Figure 8.3 tells us what the temperature in the area was in the period of the twelve images in figure 8.4. The green plot is the temperature at the weather station in Oppdal - Sæter, which is in the middle of each image in figure 8.3, while the black line represents the calculated temperature at the plateau on the upper left, Soløyfjellet. If we take a look at the temperature between week 1 and 2, we can see the temperature was below zero for both places. If we compare the two images from week 1 and 2 (April 16 and April 23, 2007) we can see the last image has a

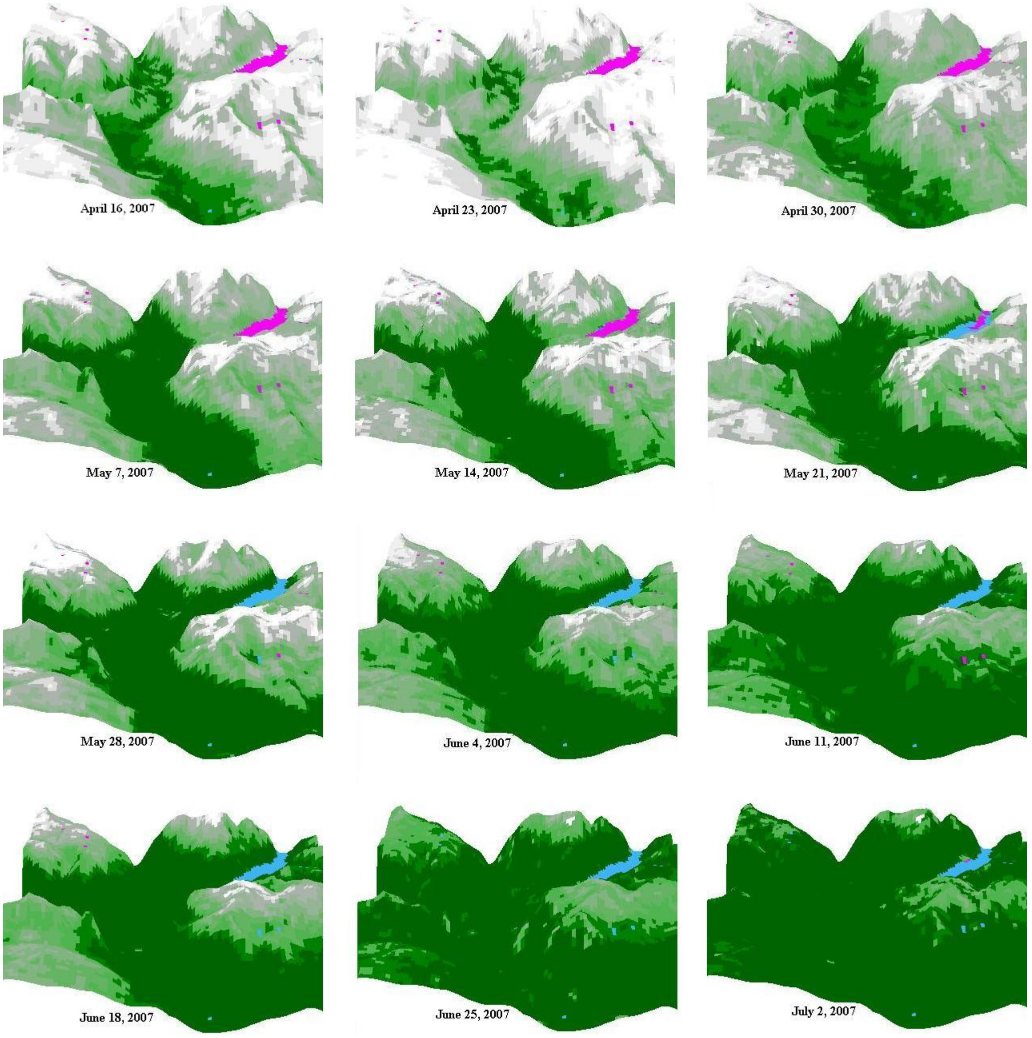

Figure 8.4: SCA-maps from the area around Oppdal. The pictures is made by putting the estimated SCA for each day on a digital elevation model. The centre of Oppdal is in the middle of these images, while Gjevilvatnet is the lake we can see on the upper right. We are looking towards west so we can see both southern and northern slopes. The images is the estimate one week apart from each other.

higher SCA. The days with temperature below zero had some precipitation, so we can assume it fell as snow, making the snow covered area bigger. The temperature on the plateau of Soløyfjellet was well above zero between week 2 and 4 (April 23 and May 7, 2007), and we can see the melting in the area has reduced the SCA in the same period. The temperature the next two weeks was lower, and we cannot

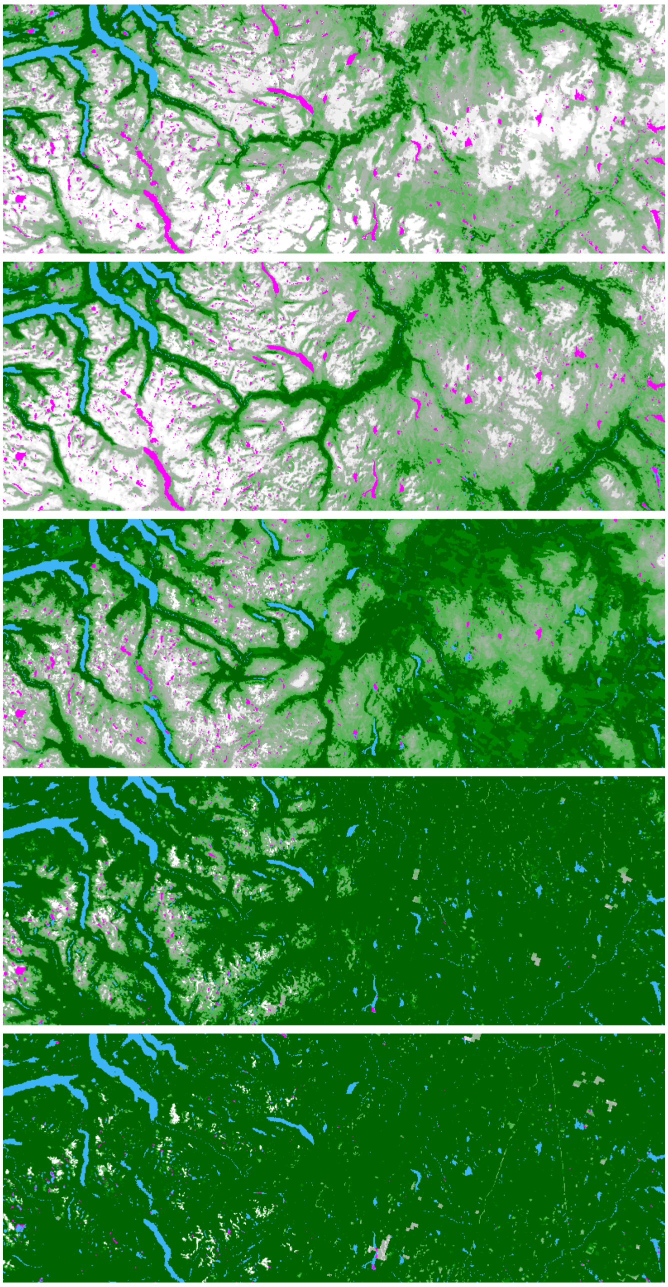

Figure 8.5: Results from the hindcasting of the measurements from 2007. The images are the estimated SCA for the first of April, May, June, July and August. Dark green is bare land, blue is water, magenta is lakes with snow cover and different shades of white is snow covered land, where white is 100% SCA.

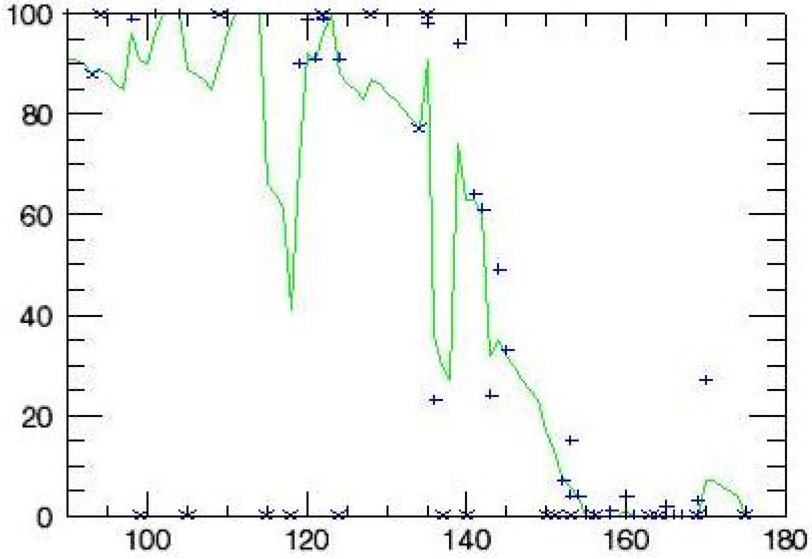

Figure 8.6: Result from using an extended Kalman filter on the MODIS and SAR measurements. The pluses are measurements done by MODIS, the x'es are measurements done by ASAR and green line is the result from the extended Kalman filter using $x_{2006}(t)$. The location of the pixel is the same as in figure 8.2.

see much melting from these pictures. From week 6 (May 21, 2007) and until week 9 (June 11, 2007) we can see the temperature again was very high, and the SCA decreased. But from week 9 to 10 (June 11 to June 18, 2007) the SCA increased on Soløyfjellet again. The temperature was again low, and the measured precipitation at Oppdal - Sæter probably fell as snow on the mountains. The period after this had high temperature, and the SCA decreased rapidly.

Figure 8.5 give us a overview over the estimated SCA for the whole area we are looking at for April 1 to August 1, 2007, with one month between every picture. We can see the snow in the western mountains stays longer than the snow in the east. Almost all lakes had ice cover on May 1, but a month later most lakes were ice free. Some noise can be seen on the two last images. More about this in section 8.6.

8.3.2 Nowcasting

It would be really interesting to be able to predict the present SCA values for all areas, not only areas where we have actual measurements. The way we tried to predict the current values for the SCA was to predict the SCA for the pixel in figure 7.1 without having the information about $x_{2007}(t)$. The algorithm used the values for past years $x_{2003}(t)$, $x_{2004}(t)$, $x_{2005}(t)$, $x_{2006}(t)$ and $x_{mean}(t)$ and checked

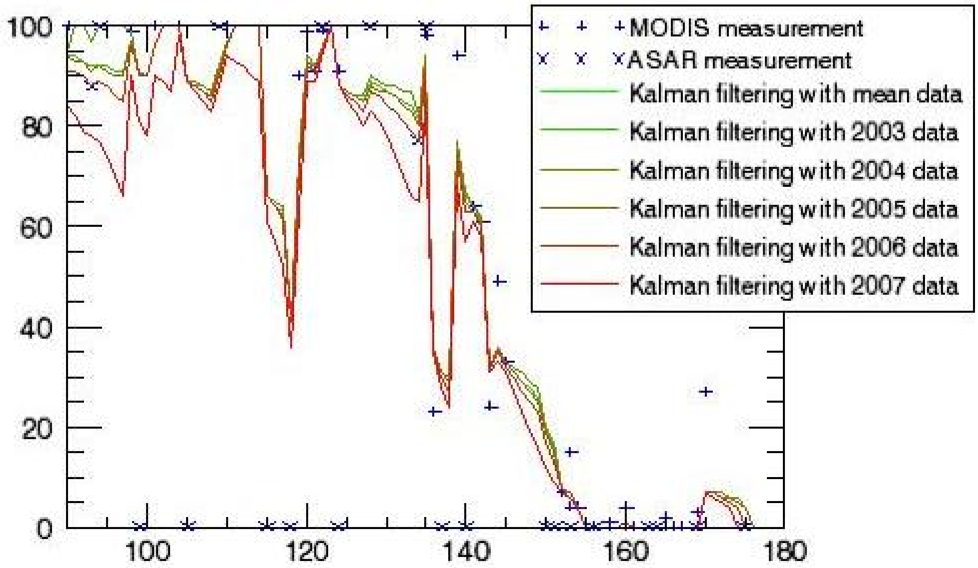

Figure 8.7: Result from using an extended Kalman filter on the MODIS and SAR measurements. The pluses are measurements done by MODIS, the x'es are measurements done by ASAR and the lines are the result from the extended Kalman filter using $x_i(t)$. The location of the pixel is the same as in figure 8.2.

which of them fitted the MODIS measurements from the same pixel in 2007. For this exact pixel, the estimate $x_{2006}(t)$ was the best fit. We see the result in figure 8.6, and if we compare it with figure 8.2 where the estimated function was based on the same measurements, there is no big difference. The estimation using $x_{2006}(t)$ is a little higher, and the snow seems to melt a little bit slower when we use $x_{2006}(t)$ compared to $x_{2007}(t)$. If we look at figure 8.7 we can see the result from the estimation using all the different $x_i(t)$. The differences is not big between these estimations, the only difference is that the estimation based on $x_{2007}(t)$ estimates the snow to melt faster than the estimation based on $x_{2006}(t)$.

The reason for this can be found if we look at the assumed functions $x_{2006}(t)$ and $x_{2007}(t)$. A figure with all $x_i(t)$ for this pixel can be seen in figure 8.8. $x_{2007}(t)$ have a much faster melting compared to $x_{2006}(t)$. Figure 8.9 give an overview over the estimated SCA for each year 2003-2007. It is clear from these figures that the snow dissapeared early in 2004, while 2005 was a year with snow laying for a long time. $x_{mean}(t)$ in figure 8.8 is also clearly an approximately mean function of the other. The estimated SCA in 2004 has two jumps in the end. This is probably because of a problem with the cloud detection, and we will look more into this in section 8.6.

Figure 8.8 shows that 2007 was the year with fastest melting, while 2004 was

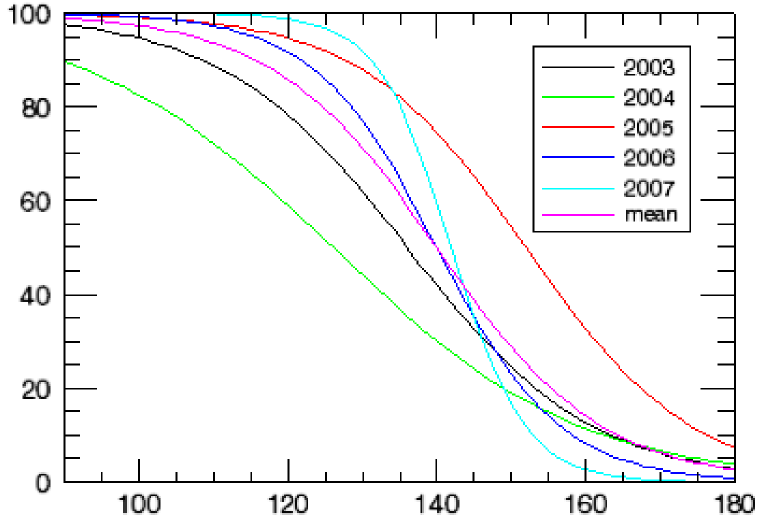

Figure 8.8: A overview over all $x_i(t)$. From this we can see that 2004 was a year where the snow dissapeared early but slowly, while the year after, 2005, the snow lasted for a long time. In 2007 the snow started to melt very late, but dissapeared very fast. The location of the pixel is the same as in figure 8.2.

the year with slowest melting. This explains why the estimated SCA in figure 8.7 is decreasing fastest when we are using $x_{2007}(t)$ and slowest when we are using $x_{2004}(t)$.

8.3.3 Spatial difference in estimating snow covered area

Our filter does not use any information about the pixels in the neighbourhood when estimating the snow covered area, only the measurements for that pixel. It is interesting to see how big difference there is in the snow covered area from one pixel to the surrounding pixels. The area we picked out to test this is an area close to the pixel used in figure 7.1. This area is relatively flat in an elevation of 940 ± 100 m. We looked at the estimated SCA in the pixel itself, the mean of the 9 closest pixels (mean SCA in an area of 750 × 750 meters), the mean of the 25 closest pixels (1250 × 1250 meters) and the mean of the 49 closest pixels (1750 × 1750 meters).

The result of these averages can be seen in figure 8.10. The difference between the estimated SCA for the middle pixel and the surrounding area is not very big. We can see the error early in the melting season is about 20% when averaging over an area of 1750 × 1750 meters, while it decreases to approximately 0% in the end. The error is smaller the smaller area we take the average over. It seems like the spatial difference in the estimated SCA is small, and there is no need for

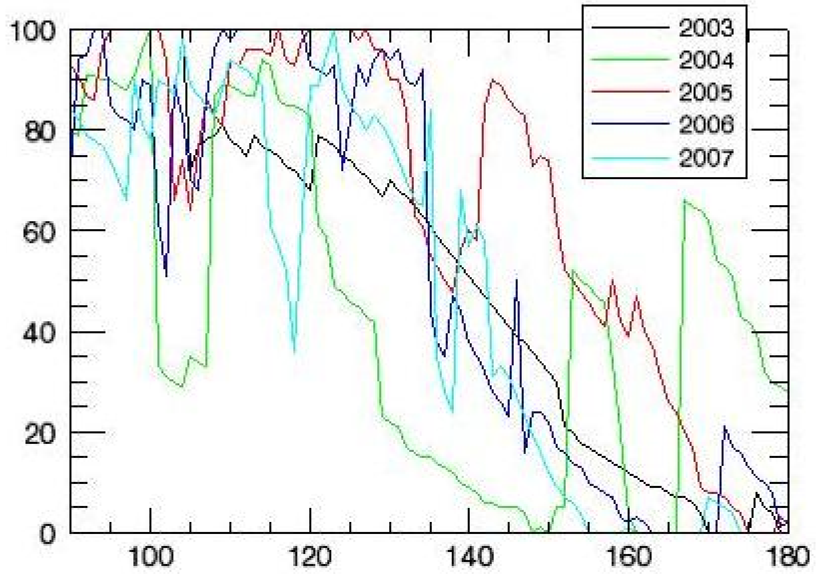

Figure 8.9: A overview over the estimated SCA for one pixel for the years 2003-2007. From this we can see 2004 was a year where the snow dissapeared early but slowly, while the year after, 2005, the snow lasted for a long time. In 2007 the snow started to melt very late, but dissapeared very fast.The location of the pixel is the same as in figure 8.2.

smoothing the result in the spatial domain.

8.4 Land cover and elevations influence on the snow covered area

The land cover mask with 36 different land cover described in section 6.1 can be used to see if there are any differences in how the snow covered area acts during the melting season. The digital elevation model (DEM) can also be used to see if the elevation has significance on how and when the snow is melting. We use all pixels in our area of 75 × 200 km where we have more than 5 MODIS measurements each year to check this. This is a total of 228397 pixels out of 241101, or 94,7% of the total area. The last 12704 pixels, or 5,3% or the area, are seas, lakes or glaciers, and as we explained in section 7.1 these pixels are treated differently. In other words; there are no pixels with less than 5 MODIS measurements for any of the years 2003 to 2007.

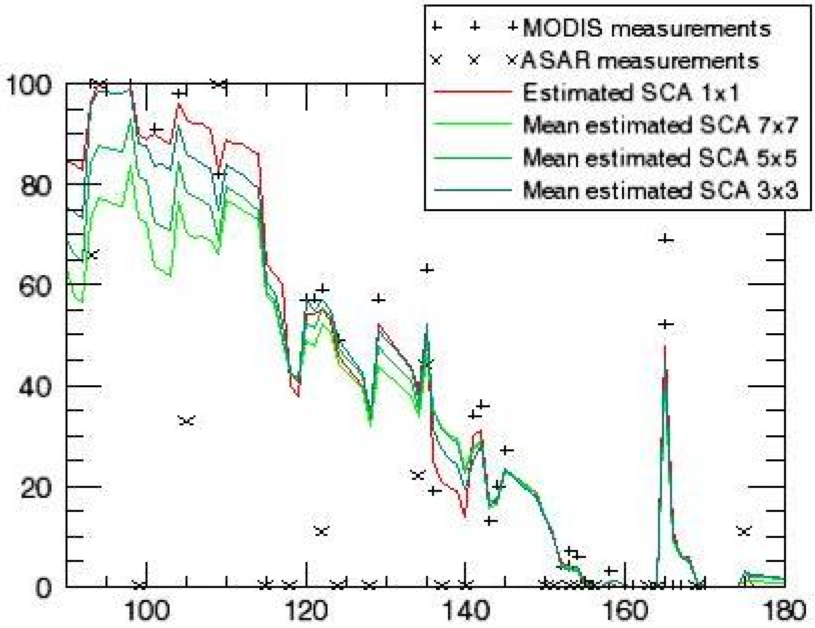

Figure 8.10: Mean estimation for SCA for 4 different sizes of area. The red line represents the estimated SCA with our extended Kalman filter for the middle pixel, while the other three lines represents the mean SCA for a larger area surrounding this pixel. The measurements represents the measurements done for the middle pixel.

If we set $t = T_0$ in equation 7.3 we get

$$\begin{aligned} x_i(t = T_0) &= 100 - \frac{100}{1 + e^{-\beta(T_0 - T_0)}} \\ &= 100 - \frac{100}{1 + e^0} \\ &= 100 - \frac{100}{2} \\ &= 50. \end{aligned} \tag{8.1}$$

This mean that T_0 can be used to see when the snow is covering 50% of the area.

Figure 8.11 shows the T_0 as a function of types of land cover. The types of land covers can be found in table 6.2. We can see the same pattern for every year which seems to indicate that there is a connection between the type of land cover and the timing of the snow melt. But if we take a look at figure 8.12, which show us the relation between T_0 and elevation we can see the same pattern. If we put these two in the same plot as in figure 8.13 we see a clear correlation.

To check this out more we may look at figure 8.14. This figure shows the mean

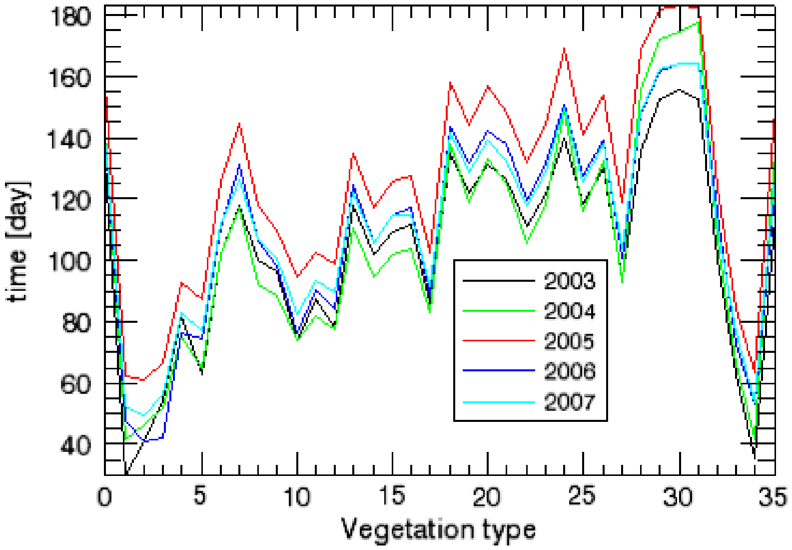

Figure 8.11: Mean T_0 for all vegatation types for the years 2003-2007 .

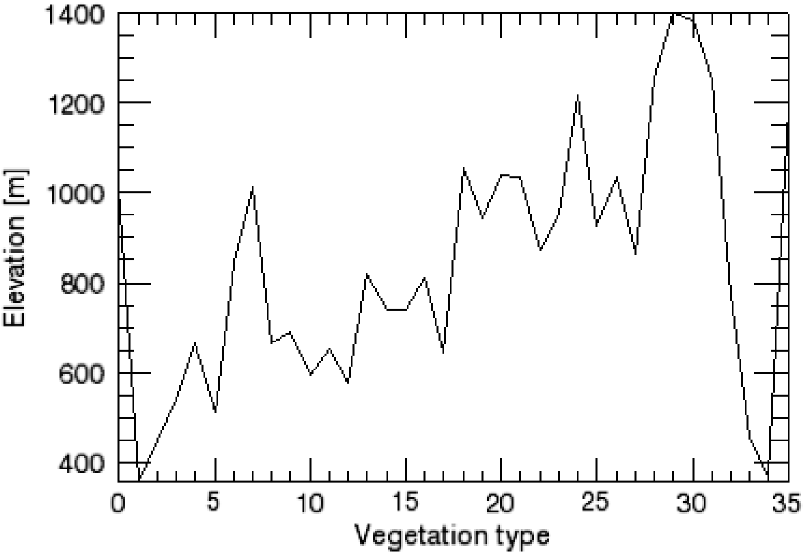

Figure 8.12: Mean elevation for all of the 36 vegetation types.

T_0 for every year for every elevation. This figure shows that T_0 is increasing as a function of the elevation. The higher a location is, the later will 50% of the snow have melted. The vegetation has small or none influence on when the melting happens.

The fluctuation in the lower and higher elevations can be explained by figure 8.15. There are few pixels at these elevations, making the T_0 being an average over

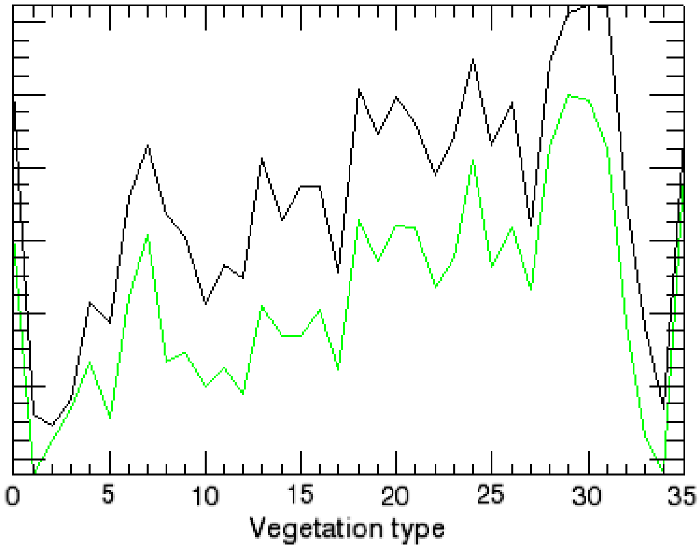

Figure 8.13: Mean elevation (green line) and T_0 for the year 2007 (black line) for each vegetation type. They are plotted together with a fictional y-axis just to see the corrolation between them.

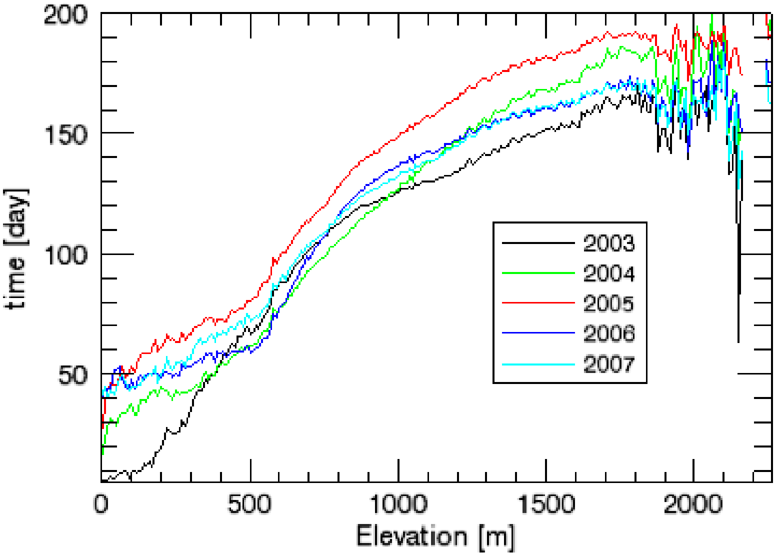

Figure 8.14: Mean T_0 for all elevations for the years 2003-2007.

less pixels and therefore being more endangered of locale variations and noise.

Some types of land cover is more common than others. Figure 8.16 shows how common each land cover is, and the least common vegetation types are type 34 (Town, cities) with 144 pixels (0,06% of the area), type 0 (Unclassifed) with

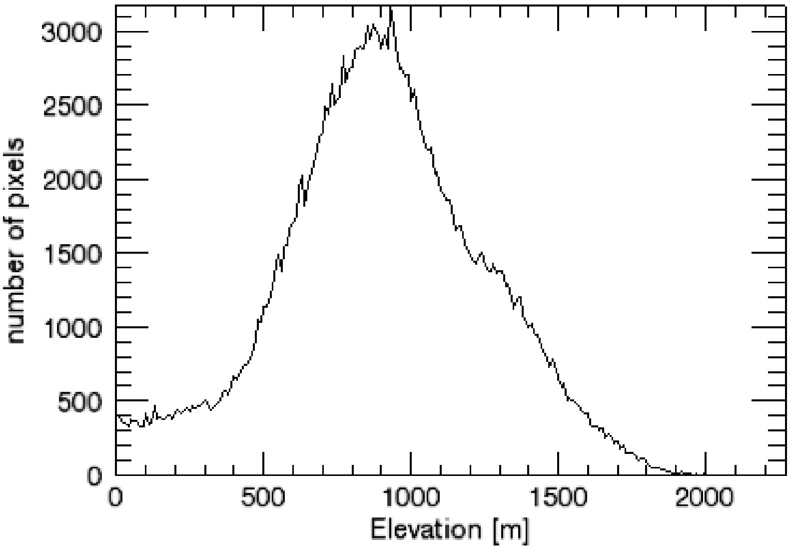

Figure 8.15: The number of pixels per elevation. The elevation is in discrete 10 meter-steps.

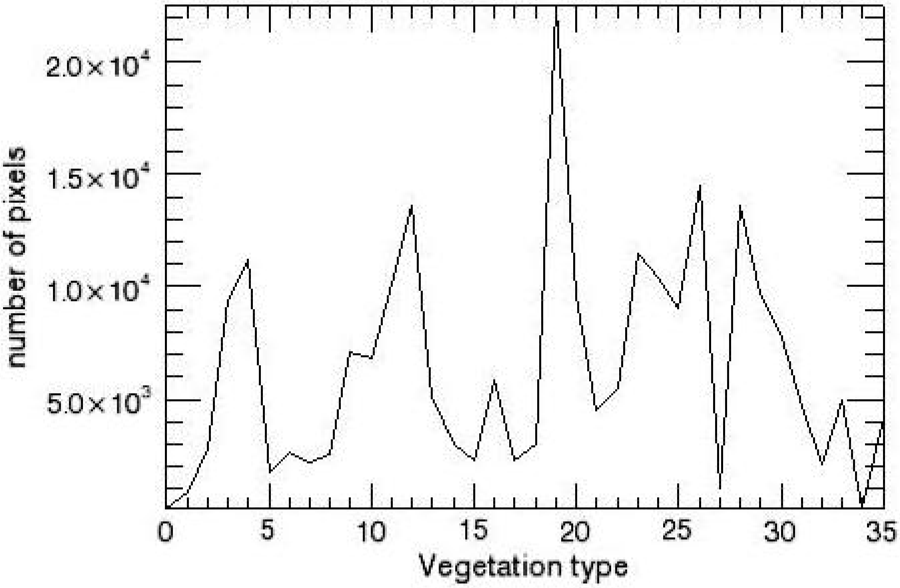

Figure 8.16: The number of pixels per vegetation type.

158 pixels (0,07%), type 1 (Spruce forest) with 879 pixels (0,38%) and type 27 (Moderate snowbed communities) with 1050 pixels (0,46%). The most common is type 19 (Open heather communities) with 22532 pixels (9,87%).

The β in equation 7.3 decides how fast the melting happens. The larger β,

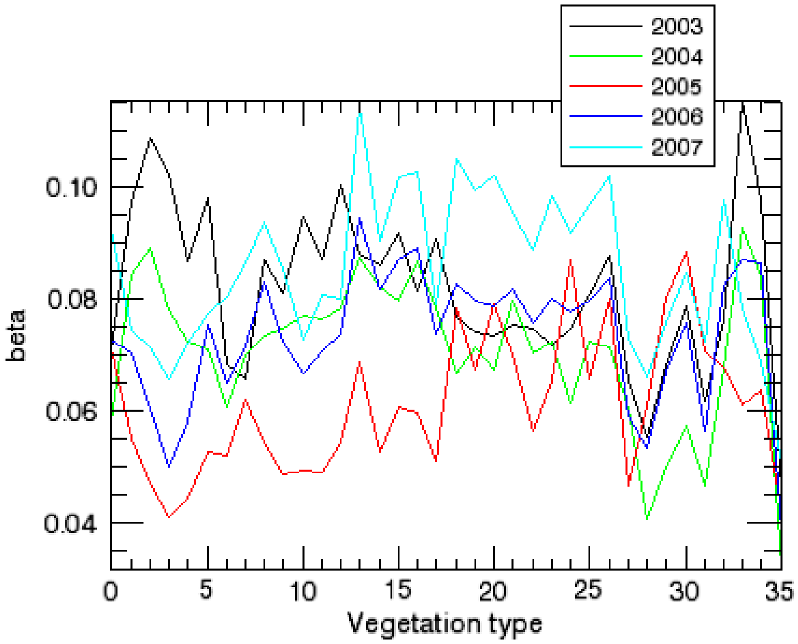

Figure 8.17: Mean β for all vegetation types for the years 2003-2007.

the faster does the melting happen. Figure 8.17 shows the mean β for all land cover types for the years 2003-2007. We see little or none correlation between each year. Only land cover type 27 (Moderate snowbed communities), 28 (Snowbeds), 31 (Snow and glaciers) and 35 (Impediment) have a generally low β. Land cover type 30 (Bare rocks and high-mountain gravel fields) has a relatively higher β than these four. Figure 8.12 indicate that all these five land cover types are found at higher elevations, and the reason for the difference in snow melting speed is probably because of the topography. Snowbeds (type 28), are usually found in areas with a lot of snow in winter time, while bare rocks and high-mountain gravel fields (type 30) usually has little snow in the winter time. It is probably not the vegetation types that make the snow melt faster, but the behavior of the snow cover which decides what kind of land cover is present.

In figure 8.18 we have plotted the mean β for all elevations for the years 2003-2007. It is not easy to see if the elevation has any impact on how fast the snow is melting, but it seems like the snow is melting slower on higher elevations. The mean β for elevations over 1700 meters are fluctuating because there are very few pixels in these elevations.

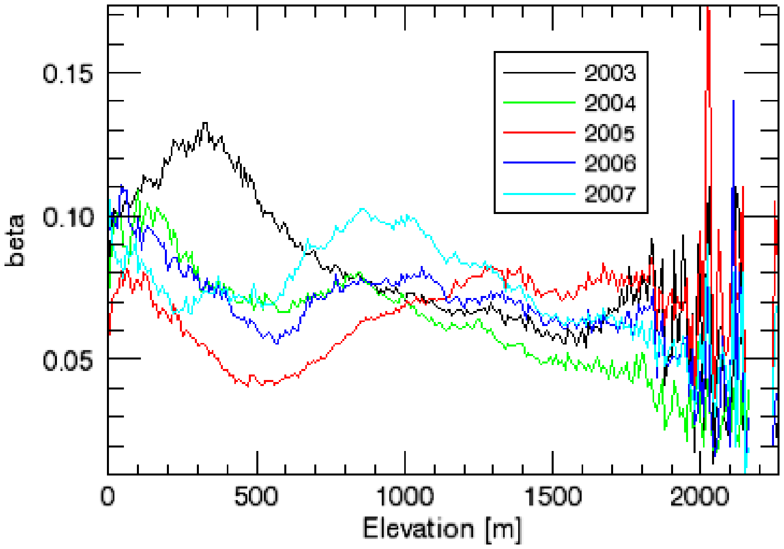

Figure 8.18: Mean β for all elevations for the years 2003-2007.

8.4.1 Problems with terrain slopes

From the perspective of an observer in middle part of Norway, the winter sun has a lower altitude in the sky than the summer sun. This means the sun will not shine as early on the northern slopes, as it will on the southern slopes. This may affect how the optical algorithm can detect snow from the MODIS images. Figure 8.19 shows the result from plotting T_0 and β for northern and southern slopes. A pixel is classified as a northern slope if the elevation of the pixel to the south is at least 10 meters higher than the pixel itself, and a southern slope if the elevation of the pixel to the south is at least 10 meters lower than the pixel itself.

The figure tells that the time when 50% of the snow is gone T_0 is generally lower for nothern slopes than southern slopes. The plots for 2003-2005 was similar to the ones from 2006 and 2007 as we can see in figure 8.19. This is an unexpected result, since it is known that snow melts earlier in southern slopes because of less shadows and higher radiation per area from the sun. The reason why we got this result is probably because the optical algorithm calculates too low snow covered area because of the shadow, making the area darker compared to other areas with the same snow fraction.

The two plots in the bottom of figure 8.19 shows how β is affected by the slopes. In both plots β has a generally lower value for the northern slopes, and the plots from 2003-2005 have the same trend. This tells us the melting takes longer time in nothern slopes than in the southern slopes. This seems to be a correct observation, since less energy will reach the northern slopes compare to southern

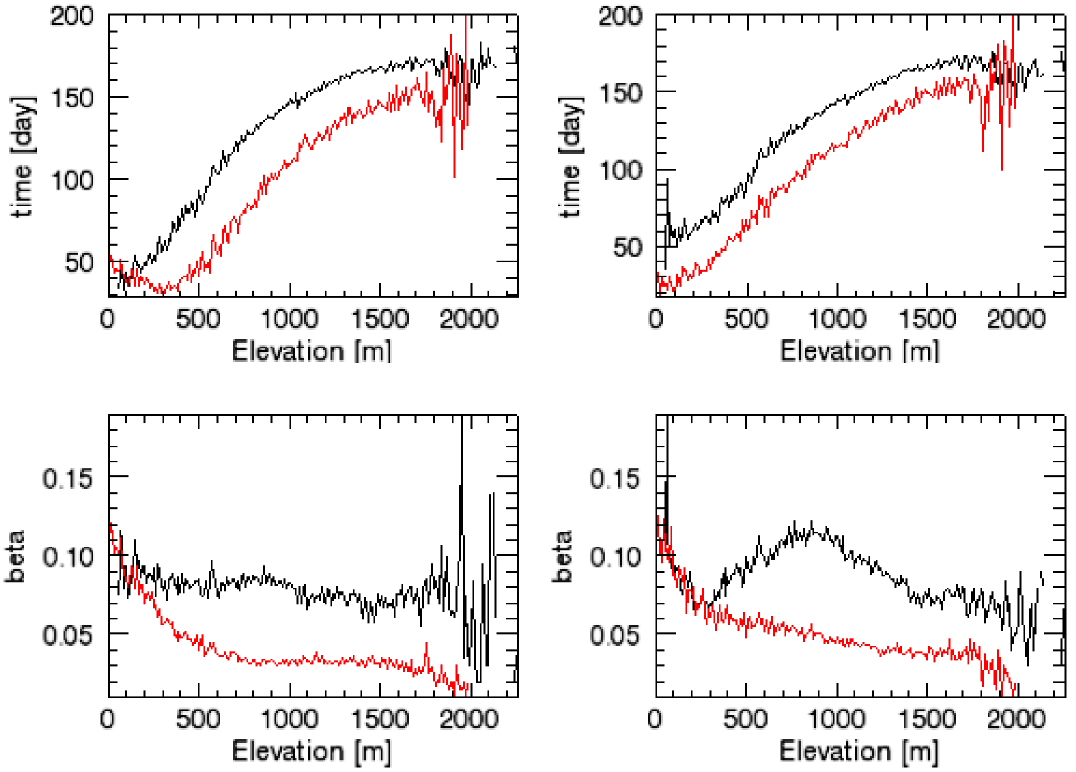

Figure 8.19: Upper left: Mean T_0 for southern slopes (black) and northern slopes (red) for all elevations for the year 2006. Upper right: Mean T_0 for southern slopes (black) and northern slopes (red) for all elevations for the year 2007. Lower left: Mean β for southern slopes (black) and northern slopes (red) for all elevations for the year 2006. Lower right: Mean β for southern slopes (black) and northern slopes (red) for all elevations for the year 2007.

slopes because of the low altitude of the sun.

8.5 Comparing the results with meteorological measurements

In section 6.2 we presented some meteorological measurement stations in the area we are looking at. These stations will give us information about temperature, precipitation, snow depth and in situ snow covered area-estimates, and can help us to evaluate the results we have got.

Figure 8.20 is showing the estimated SCA from our extended Kalman filter, the temperature measured at the station, snow depth, precipitation and in situ

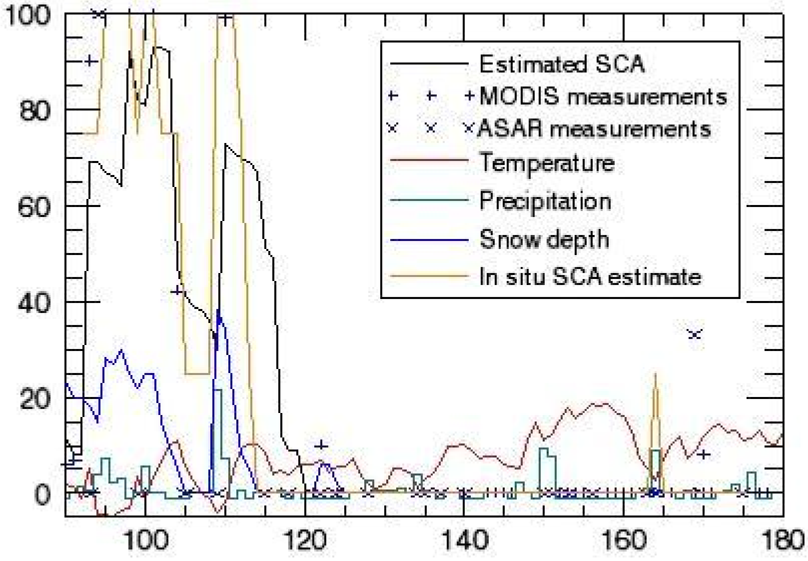

Figure 8.20: Measurements and estimates from Oppdal - Sæter measurement station. The estimated SCA is done by our extended Kalman filter. The estimations of SCA is in %, Temperature is in °C, precipitation is in mm and snow depth is in cm.

SCA estimate from the measurement station in Oppdal - Sæter. Our estimated SCA seems to fit the temperature measurements. The mean temperature is above zero from day 101 (April 12, 2007), and the estimated SCA is decreasing fast from day 103 (April 14, 2007). The reason for this delay is that there were no measurements the days before, but the mean temperature is also low the days before, so the melting would have been slow. On day 109 (April 20, 2007) the temperature was again below zero, and the precipitation fell as snow. The day after (April 21, 2007), MODIS estimated the SCA to be 99%, and our extended Kalman filter estimated the snow cover to be much higher again. On the next days the temperature was high again, and the snow melted fast, but our filter estimated the snow to be higher than what it was according to the meteorological observations. The main reason for this was few measurements these days.

Figure 8.21 shows the estimated snow from the measurement station in Tingvoll - Hanem. It is a measurement station close to the sea, and as we see in the figure, there were not much snow, and the temperature is generally higher than in Oppdal - Sæter in figure 8.20. There are only in two short periods there are any meteorological observations of snow cover, and in these periods there are only one MODIS measurement and one ASAR measurement in each. MODIS did not measure 100% SCA in any of these periods, even when it was 21 cm snow depth in the first period. The result from this is an estimate with less snow than measured

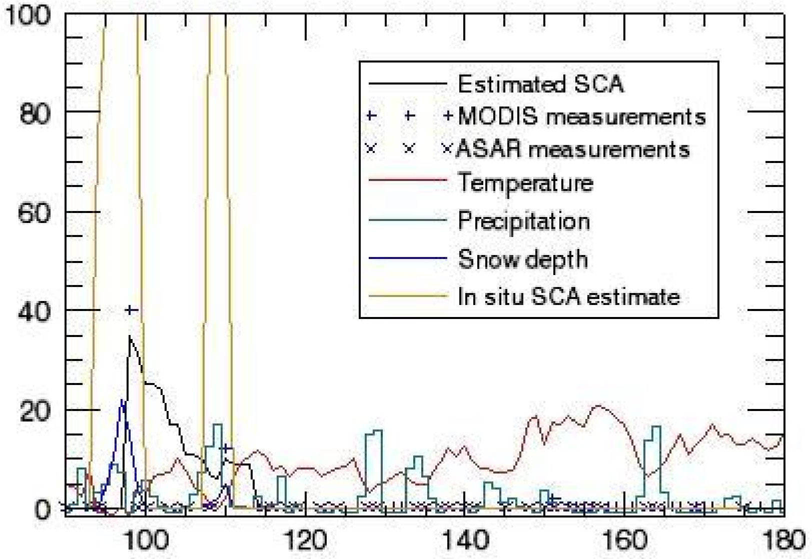

Figure 8.21: Measurements and estimates from Tingvoll - Hanem measurement station. The estimated SCA is done by our extended Kalman filter. The estimations of SCA is in %, Temperature is in °C, precipitation is in mm and snow depth is in cm.

in situ, and a longer melting period since there are few measurements.

Figure 8.22 shows the measurements and estimates from Røros Airport. Røros is about the same elevation as Oppdal, but in a dryer and generally colder climate. The days when the temperature is above zero correspond very well with the days when our filter estimates the snow to melt.

The in situ SCA estimate is not something that should be fully trusted. The observations are subjective but probably based on experience and there are only 5 SCA-steps which make the error high. What is better to trust is the temperature and the precipitation. It can give us valuble information on how the SCA evolves over time.

8.6 Problems with detection of clouds with MODIS

The snow retrieval algorithm used for MODIS has a problem with detecting clouds. In figure 8.23 we can see an example of this. On July 9, 2007, we can see that there are very little snow in the whole area. There is only some remaining snow on the mountains in the west. The next day, on July 10, 2007, there has appeared several squared areas with some snow, and even a lake with partially snow cover in the west. The reason for this weird result can be found by looking at the measured

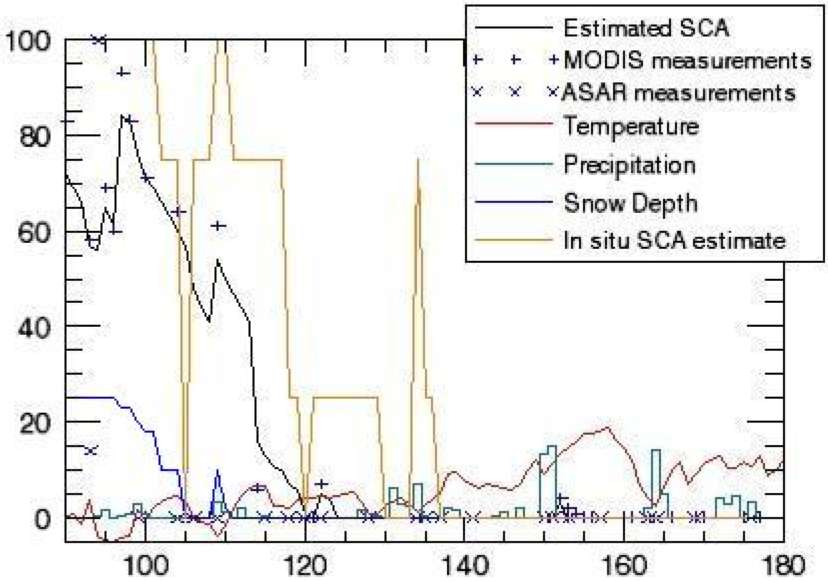

Figure 8.22: Measurements and estimates from Røros Airport measurement station. The estimated SCA is done by our extended Kalman filter. The estimations of SCA is in %, Temperature is in °C, precipitation is in mm and snow depth is in cm.

snow cover done by MODIS on July 10, 2007 in the bottom of figure 8.23. The whole area is covered with clouds, only some small spots has gone through the cloud detection algorithm as no-clouds. These spots has got a relativelly high snow cover fraction from the snow cover algorithm, which is very unlikelly at these places in the middle of July. The weather measured by the Norwegian Meteorological Institute in Oppdal this day was a middle temperature of 11,3°C and 13,7 mm of precepitation in form of rain. Also at Rorøs the temperature was 11,7°C with 21,4 mm of precepitation, so the chance of this actually being snow is very low.

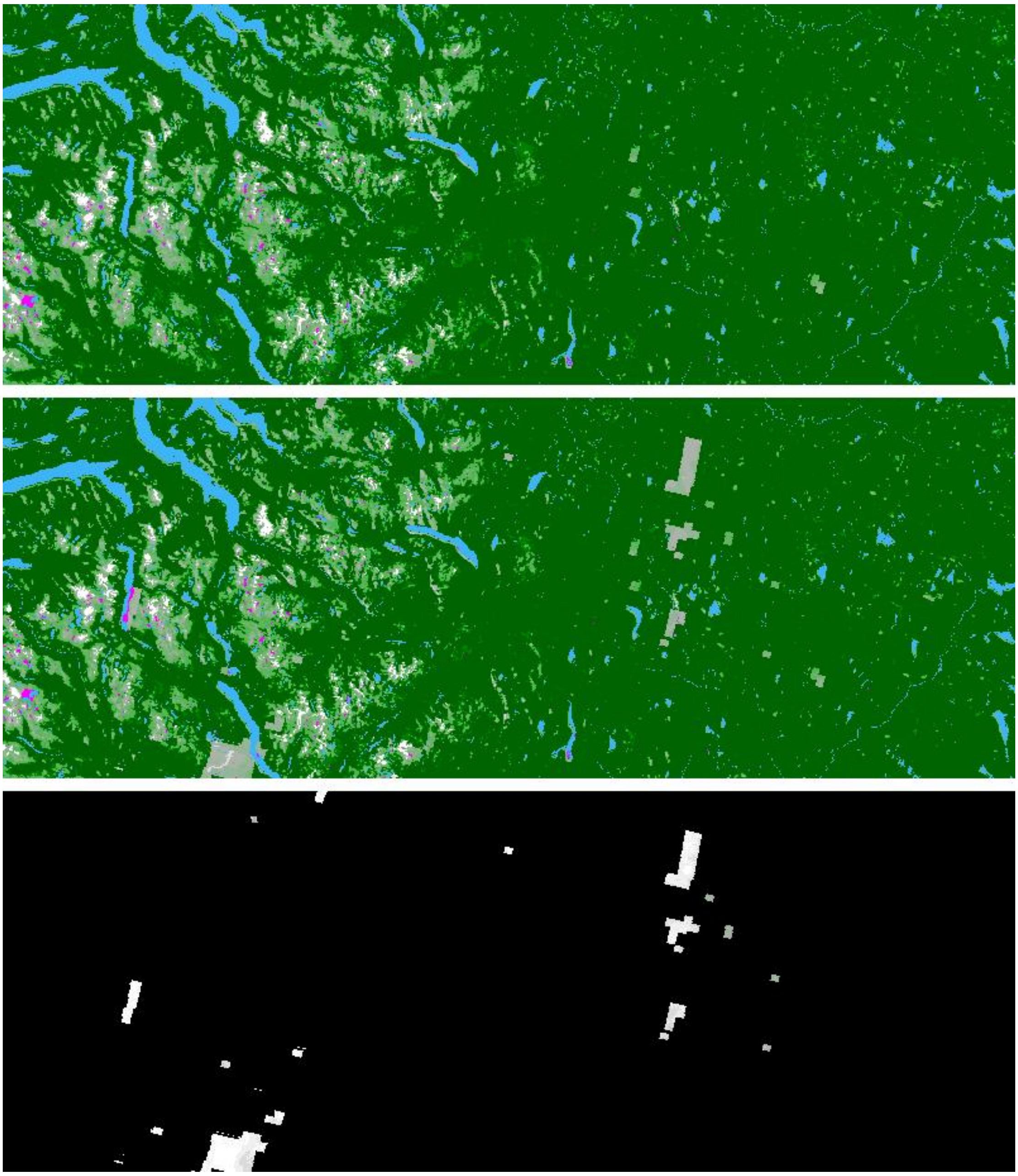

Figure 8.23: Top: Map over estimated snow covered area on July 9, 2007. Blue is water, magenta is water with snow cover (must likelly erroneous), dark green is bare ground, and lighter green up to white is snow covered area. The more light green, the higher percent SCA. Middle: Map over estimated snow covered area on July 10, 2007. Bottom: Measurement done by MODIS on July 10, 2007. Black is clouds masked out, while white is snow covered area.

Chapter 9

Conclusion

In this thesis we have studied how SCA-maps are made from satellites using two different instruments. We have described the pros and cons for each instruments. We have filtered these maps using two different filters, and especially studied the Kalman filter for this purpose. We have also studied the relation between elevation and snow covered area and a land cover map and snow covered area. We found that the extended Kalman filter gave a clear improvement when compared to the simple moving average filter. We also found that the extended Kalman filter worked well for both hindcasting and nowcasting of snow covered area, even in areas with no measurements the last days.

The spatial difference in the estimations seems small, and the vegetation does not seem to influence the way snow are melting. The elevation has a high influence on when the snow is melting. We tried to study differences in melting at north and south slopes, but found that the data were not good enough. The error was created in the optical images because of shadows in the northern slopes. Since the snow calibration areas with 100% snow is located on top of glaciers plateaus, which are horizontal, shadows will make the optical algorithm underestimate the snow covered area. The snow cover in southern slopes are melting faster than the snow cover in the nothern slopes, and this is correct since the sun radiate more energy to southern slopes, and therefore melting the snow faster. The filtered estimation of the snow cover fits the measured temperature and precipitation on nearby weather station very well as long as there are regular measurements.

The biggest problems with the estimation of SCA was the erroneous input from the snow cover retrieval algorithms. The ASAR sensors has problems detecting dry snow, while the MODIS sensors cannot see through clouds, and the algorithm applied on the measurements is misinterpreting the clouds as no clouds some times.

9.0.1 Further work

Some issues that should be developed further are:

- In thesis we used satellite measurements only to estimate the snow covered area. Since clouds are common in the melting season and the ASAR does not cover all areas every day, we may have several days without new input. This makes the error in the estimation high. Additional input is needed, and the two most obvious is temperature and precipitation. Both can be obtained from weather station all over the country, and temperature maps like the one in figure 5.3 can be used to find out if the snow is melting or not. The precipitation together with the temperature map can be used to predict an increased SCA.
- The dry snow cover algorithm can be improved as well. One way is to compare the snow cover with earlier measurements as well as information about temperature in the same period.
- The detection of clouds in MODIS measurements does also need improvement. A solution can be to compare the snow cover with the earlier measurements as with the problems with the dry snow cover algorithm.
- Even if the spatial difference in SCA does not seem big, it may be an idea to see if this will improve the SCA-maps even more.
- As showed, the optical algorithm has problems detecting snow correctly in nothern slopes. The slopes has high influence on the melting of snow, and it may be worth to take a look into solution for compensating for this.

Bibliography

[1] A. Almendral-Vazquez and A. R. Syversveen, 2006. "The Ensemble Kalman Filter - theory and applications in oil industry". Report SAND/05/06, Norsk Regnesentral, 12 September 2006. http://publications.nr.no/enkal.pdf

[2] T. Andersen, 1982. "Operational snow mapping by satellites". Hydrological aspects of alpine and high mountain areas, Proceedings of the Exeter symposium, July 1982, IAHS publ. no. 138, oo. 149-154.

[3] N. Baghadi, Y. Gauthier and M. Bernier. "Capability of multitemporal ERS-1 SAR Data for Wet-snow mapping". Remote Sensing of Environment, Volume 60, Number 2, May 1997, pp. 174-186.

[4] R. E. Dickinson, 1995. "Land processes in climate models", Remote sensing of Environment, Vol. 51, pp. 27-38.

[5] C. Elachi and J. van Zyl. "Introduction to the Physics and Techniques of Remote Sensing", 2 ed., Wiley-Interscience, 2006.

[6] R. O. Green and J. Dozier, 1995. "Measurement of the spectral Absorption of liquid water in melting snow with an imaging spectrometer". Summaries of the Fifth Annual JPL Airborne Earth Science Workshop, 23-26 January 1995, JPL Publication 95-1, pp. 91-94.

[7] R. B. Huseby and R. Solberg, 2005. "A model-based approach for geometric correction of optical satellite images". International Journal of Remote Sensing, In press.

[8] J. R. Jensen, "Remote Sensing of the Environment, An Earth Resource Perspective". 2 ed., Pearson Education, Inc 2007.

[9] B. E. Johansen and S. R. Karlsen. "Vegetation mapping of Norway, using Landsat TM/ETM+ data". Norut-Troms.

[10] R. E. Kalman, 1960. "A New Approach to Linear Filtering and Prediction Problems". Transaction of the ASME - Journal of Basic Engineering, pp. 35-45, March 1960.

[11] J. T. Koskinen, J. T. Pulliainen and M. T. Hallikainen. "The use of ERS-1 SAR data in snow melt monitoring". IEEE Transaction on Geoscience and Remote Sensing, Vol. 35, No 3, May 1997, pp. 601-610.

[12] E. Malnes and T. Guneriussen. "Mapping of snow covered area with Radarsat in Norway". Geoscience and Remote Sensing Symposium (IGARSS), Vol. 1, June 2002, pp. 24-28.

[13] C. Mtzler and E. Schanda. "Snow mapping with active microwave sensors". International Journal of Remote Sensing, Vol. 5, pp. 1521-1523, March/April 1984.

[14] T. Nagler and H. Rott. "Retrieval of Wet Snow by Means of Multitemporal SAR Data". IEEE Transactions of Geoscience and Remote Sensing, Vol. 38, No. 2, March 2000, pp. 754-765.

[15] T. Nagler, H. Rott, E. Malnes, R. Storvold, K. Luojus, J. Pulliainen, M. Hallikainen and P. Pampaloni, 2005. "Development of algorithms for Snow Covered Area (SCA) retrievals from SAR data". Project report for EU, Deliverable No. 6, D6-WP2, project EnviSnow EVG1-CT-2001-00052, 2005.

[16] T. Nagler, H. Rott, P. Pampaloni, E. Malnes and M. Hallikainen, 2003. "Radar Remote Sensing of Snow and Soil Parameters". Project report for EU, Deliverable No. 5, D1-WP2, project EnviSnow EVG1-CT-2001-00052, 2003.

[17] W. G. Rees. "Remote Sensing of Snow and Ice". Taylor & Francis Group, 2006.

[18] R. Solberg and T. Andersen. "An Automatic System for Operational Snow-Cover Monitoring in the Norwegian Mountain Regions". Geoscience and Remote Sensing Symposium (IGARSS), Pasadena, California, USA, 1994.

[19] R. Solberg, J. Amlien, H. Koren, L. Eikvil, E. Malnes and R. Storvold. "Multi-sensor and time-series approches for monitoring of snow parameters". IEEE International Geoscience and Remote Sensing Symposium (IGARSS 2004), Anchorage, Alaska, USA, 20-24 September 2004.

[20] R. Solberg, J. Amelien, H. Koren, L. Eikvil, E. Malnes and R. Storvold. "Multi-sensor/multi-temporal snow cover area algoritms". Project report for

EU, Deliverable No. 9, D1-WP3, Part 1, project EnviSnow EVG1-CT-2001-00052, 2005.

[21] R. Storvold, E. Malnes and I. Lauknes, 2005. "Using Envisat ASAR Wideswath data to retrieve snow covered area in mountainous regions".

[22] G. Welch and G. Bishop, 2006. "An Introduction to the Kalman Filter". http://www.cs.unc.edu/∼ welch/media/pdf/kalman_intro.pdf.

[23] External access to climatedata from Norwegian Meteorological Institute, http://eklima.met.no

[24] D. Herring, NASA Earth Observatory, http://eobglossary.gsfc.nasa.gov/Study/ArcticReflector/

[25] The Landsat-7 Science Data User's Handbook, http://landsathandbook.gsfc.nasa.gov/handbook/handbook_toc.html

[26] MODIS Webiste, http://modis.gsfc.nasa.gov/

[27] Norge Digitalt, Nasjonal geografisk infrastruktur, http://www.statkart.no/Norge_digitalt/Norsk/Basisdata/Hoydedata/